Karlsruher Institut für Technologie

VERSUCHSANSTALT
FÜR STAHL, HOLZ & STEINE

Diplomarbeit

zum Thema

Simulation of the welding process of steel tube joints made of S355 and S690

vorgelegt von: cand. ing.
Janna Krummenacker

Erstprüfer: Univ.-Prof. Dr.-Ing. T. Ummenhofer
Zweitprüfer: Univ.-Prof. Dr.-Ing. H. Blass

April 2011

Preface

This diploma thesis has been carried out during an Erasmus exchange at the Steel Structures Laboratory (ICOM) at the École Polytechnique Fédérale de Lausanne (EPFL).

First, I would like to thank my supervisor Professor Thomas Ummenhofer who supported the idea of an exchange and initiated the contact with Professor Alain Nussbaumer, whom I would like to thank for his continuos and highly qualified support. The regular meetings and his questions always helped me very much to progress with my work. I would also like to express my sincere gratitude to Farshid Zamiri for his dedicated mentoring and competend assistance with all my questions. Thank you very much to Claire Acevedo, whose experience in the field of welding simulation and advice was very helpful and simplified the start of my work a lot. I also would like to thank the entire ICOM staff for their cordial welcome.

Thank you to Professor Andreas Mortensen and the Laboratory of Mechanical Metallurgy (LMM) for the provision of the tensile testing machine. I also would like to thank Willy Dufour and Gilles Guignet for their assistance and help during the set-up of the machine and the experiments.

Lastly, I would like to thank my friend Mariette Martin for the great and time-consuming editing of my work.

Abstract

Welding is an important joining method for the work with metals. During the welding process, the material is heated and deforms plastically which leads a change in microstructure in the heat affected zone, to complex residual stress distributions, and distorsions. The residual stresses can have a major impact, among other phenomena, on the fatigue resistance of a welded structure. The aim of this work was to develop a model with the finite element software Abaqus for the simulation of a welding process for butt welded tubes and the calculation of the resulting welding residual stress field.

The residual stress field depends on several input parameters, like the geometry, the heat input, the welding speed, the material data, and the number of weld passes. The chosen dimensions of the tubes are realistic for tubular steel bridge constructions. Since, no experimental welding procedures were conducted, the welding parameters like the heat input and the welding speed were estimated in order to obtain a realistic temperature distribution in the weld and the heat affected zone. The assignment asked to place a main focus on the influence of the material data and the number of weld passes.

Within the framework of this work, tensile tests at three different temperatures were conducted in order to find the deformational behavior of the two different steel grades S355 and S690. The results show generally good agreement with the data given by the European Standard for the structural fire design of steel structures [11], that is noted Eurocode 3 (EC3) in the course of this work. According to the test results, the yield strength at room temperature are underestimated by the Eurocode 3.

Based on the experiments and the data given in the Eurocode 3, the influence of the mechanical properties were studied in several Abaqus models. For the description of the temperature dependent material behavior, a bilinear stress-strain curve was implemented. The resulting stress distributions show a similar trend, but the offset values between the stress curves of two models are dependent on the position in circumferential direction and the distance in axial direction. During the literature study, different welding simulation programs were compared. With specific welding simulation programs, mostly two-dimensional models can be realised. A major advantage of these programs is, that phase transformations can easily be considered and therefore a more realistic material model can be implemented provided that the temperature dependant behavior of the different microstructural phases are known.

The influence of the number of weld passes was studied by comparing a single- and a multi-pass model with the material data from the Eurocode 3. The total heat input and the welding speed was the same for all the models. The tendency of the resulting stress distributions varied greatly and therefore implies that a multi-pass model cannot be approximated by a singlepass model.

Contents

List of Figures

List of Tables

Chapter 1

Introduction

Steel is one of the most common construction materials and widely used for the design of taller buildings, bridges, cranes, and hydraulic steelworks as well as industrial buildings. Compared to other construction materials it has very good properties regarding its ductility, strength as well as its homogeneous and isotropic microstructure. A significant advantage of steel is its small ratio of volumetric weight to strength, which is especially true for high strength steels. From a materialistic point of view, it is an alloy of iron and carbon with a maximum carbon content of 2.06 % [3]. With increasing carbon content the steel becomes harder and stronger, but also its ductility decreases, which is why this carbon limit has been established. Furthermore, an increased carbon content leads to a degradation of the weldability. By the use of other alloy elements as silicon, manganese, chromium, vanadium, and tungsten, the material properties can be influenced, in order to obtain various steel types for a wider application area. Structural steels are low alloy steels with a carbon content below 0.7 %.

In this work, two structural steels are used with different yield strengths. The steel type S355 is a common steel grade and used for wide applications fields, whereas grade S690 is defined as high strength steel and has recently started to play an increasingly important role in the field of steel construction. The fatigue proof for steel structures in the Eurocode 3 [12] is only dependent on the notch type and therefore not on the steel type. This is the reason high strength structural steels are only advantageous when the proof of fatigue strength is not governing.

For the dimensioning of steel structures, a main focus is placed on the connections between the individual steel parts. Along with bolted connections, welding is one of the most important connection type. During the welding process, the material is heated to temperatures above the melting point. The molten material forms a weld pool, sometimes with the use of filler material resulting in a joint after the cooling of the material. The main advantages of a welded connection as oposed to other fastening methods is the use of less material, thus weight savings, and effective load transmission. Additionally, repairs can easily be realized with the use of welding. A major disadvantage is, that welds often contain defects, that are hard to detect and therefore welding requires expertise and trained specialists. The extreme and localized heat input results in microstructural transformation in the heat affected zone as well as heat distorsion. Another unfavorable condition of welded joints is the creation of a permanent joint, that cannot be replaced later.

During the welding process, the material is heated and thus plastically deformed. This provokes residual stresses, that depending upon their sign, magnitude, and distribution can either be detrimental or beneficial. When the residual stresses act in the same direction as the load stresses they can significantly reduce the maximum capacity load, whereas when they act

in the opposite direction plastic deformation generally occurs later and the maximum load is therefore increased. The residual stress distribution is also of special interest for constructions under dynamic load. This is the reason for the high impact of reliable residual stress prediction on accurate fatigue assessment. By adjusting the welding parameters and the use of post-weld heat treatments, the weld quality should be optimized to avoid residual stresses, distorsions and weld defects.

The experimental study of the impact of the numerous welding parameters is an expensive and time-consuming effort, whereas numerical simulations present an alternative. In this work, the prediction of residual stress distributions in butt-welded tubes is studied by the use of numerical simulation. The models are created and analysed with the finite element software Abaqus. The main disadvantage of numerical simulation is the limitation of computational power and calculation time. Therefore, numerical models require the implementation of many simplifications that can falsify the results of the analysis. The finite element model requires a spatial and time discretization, which also influences the accuracy of the results.

For the residual stress determination it is not only fundamental to use realistic welding parameters, but also to employ material models that are realsitic for the behavior at elevated temperatures. The needed properties are often not available in the literature. For the common steel types used in constructions (like S235 and S355) investigations of the material behavior at high temperatures and numerical welding simulations have been published by Loose [27] and Wichers [47]. For high strength steel, even less publications regarding the material properties at elevated temperatures have been made and the only experimental determination of the mechanical properties of S690 known to the author, were conducted by Outinen [29]. This is why, in this work, tensile tests with specimens made of S355 and S690 are conducted in order to find the stress-strain curves at elevated temperatures.

The welding simulation and residual stress determination for welded tubes mostly focuses on pipe systems or the tubular structures of offshore platforms. But tubular steel trusses are also used for bridge design, where different dimensions and steel types are employed as previously mentioned. This is the reason why it is difficult to draw conclusions from welded piping systems for the residual stress distributions in other structural applications. Combined with high strength structural steel, tubular steel trusses allow a slim bridge design combined with high load capacity as e.g. in the construction of the Millau Viaduct, 12000 tonnes of the high strength steel S460 were used [43]. Since the implementation of the Eurocode 3, Part 1-12 [13] in 2007, the Eurocode 3 is extended to steel grades S700 which has simplified a wider application of high strength steel in construction.

Chapter 2 presents the state of knowledge for residual stresses and the material properties used during the thermal and mechanical simulation for the steel grades discussed in this work. Also, the general approach for welding simulation is explained with reference to the literature. Furthermore, some well-established simulation programs are listed and compared.

The experimental data is presented in Chapter 3. First the test set-up, the specimen type, and the test matrix are described followed by the discussion of the results.

In Chapter 4 the theory of a finite element welding simulation and a subsequent residual stress calculation is presented. The thermal and mechanical material properties used for the numerical simulations are presented as well as the applied thermal and mechanical boundary conditions.

The different Abaqus models are described in Chapter 5. First the implementation of a verification model and the resulting residual stress field is described. Secondly, the results of four models are presented and compared, with a main focus on the influence of the yield strength and the influence of the number of weld passes on the residual stress distribution.

Chapter 2

State of knowledge

2.1 Welding temperature field

The concentrated and transient heat input of the welding source combined with the thermal material properties creates a temperature field with temperatures in the range of the ambient temperature to 3000°C, the evaporation temperature of steel. In this temperature range, the material is experiencing various microstructural transformations and thus different zones can be distinguished depending on the isothermal lines occuring around the heat source:

- the weld pool, where the base metal and the filler material are fused
- the heat affected zone (HAZ), where the material is not molten but due to the heat input micostructural transformations occur and change the material properties
- the base metal, that is not influenced by the elevated temperatures

The iron-carbon phase diagram depicts the phase compositions of steel at different temperatures depending on the carbon content. The diagram is fundamental for understanding the phase transformations of iron-carbon alloys during heating and cooling. Fig. 2.1 illustrates the relevant part for structural steel of the simplified iron carbon diagram. The microstructure of the heat affected zone (HAZ) of welded plates made of S355 was analysed by Wichers [47]. The feritic-perlitic microstructure of the base metal is transformed to austenite for temperatures above the upper transformation point A_3. Between the lower A_1 and the upper transformation point the structure is partially austenitic. This transformation results in a coarser microstructure which leads to diminished toughness properties in the HAZ. This is why alterations in the mechanical behavior have an impact on the fatigue life of a structure. Therefore it is also important to analyse the temperature field and not only the residual stress field.

For high strength structural steel like the steel type S690, little research concerning welding simulation has been published so far. Hildebrand [18] states that it is very important to include microstructural transformations in the welding simulation with high strength steel. In his work, the material properties are modeled as a compound of different microstructures that react individually under temperature changes. The initial microstructure of S690QL is composed of bainite and martensite which is completely transformed into austenite at temperatures above the A_{c3}-temperature. The microstructural transformations depend on temperature as well as on time. Thus, the finally formed phases can be predicted by the use of a Time-Temperature-Transformation diagram (TTT). A TTT diagram for S690 can

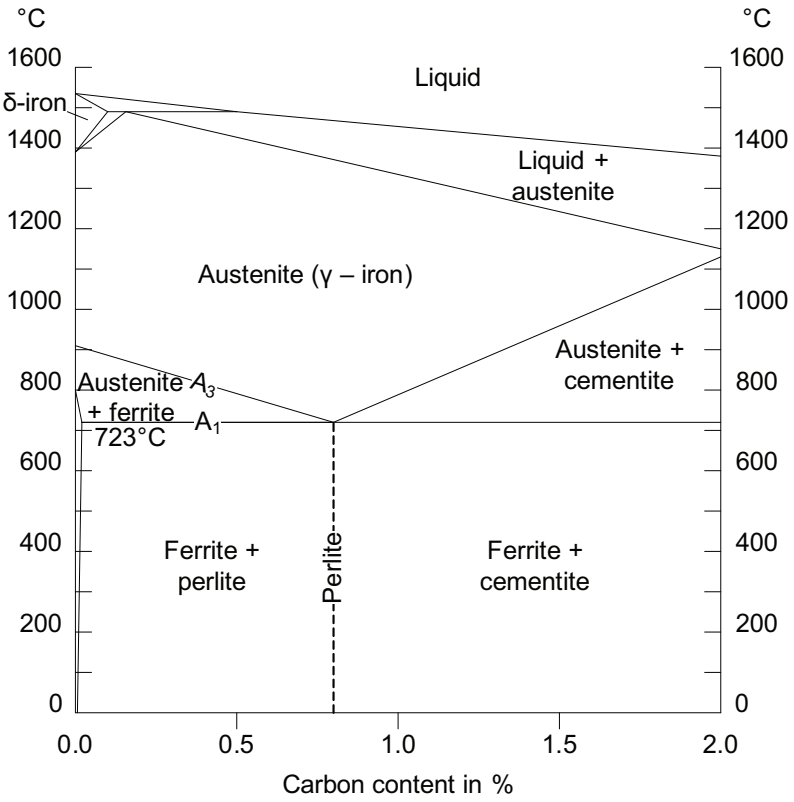

Figure 2.1: part of a simplified iron-carbon diagram

be found in the work by Hildebrand [18]. The martensitic and the bainitic phase in the heat affected zone are partially transformed into low strength steel which makes it important to include microstructural transformations into simulations with high strength steel. The fatigue strength can be augmented by post-weld heat treatments [44]. For high strength structral steel, various methods were investigated and are discussed by Kuhlmann et al. [20].

In welding simulations, the complex process of the welding arc is simplified and only the effect on the material is modeled by applying a heat input. The form of the heat source needs also to be simplified and adapted to the simulated welding procedure. The applied welding method in this work is metal active gas (MAG) arc welding. In the arc welding methods, the heat is produced by electrones and ionic gas molecules that impinge on the anode and the cathode respectively. For arc welding, the most suitable heat source model seems to be the double ellipsoidal form with a Gaussian distribution of the power density presented by Goldak and Akhlaghi [17].

The fundamental equation for the temperature field, that is produced by the heat input of the welding arc, is the heat conduction law. In chapter 4 it will be presented in detail.

2.2 Residual stresses

Residual stresses are internal forces, that are at equilibrium with themselves and occur without external forces acting [33]. They can be caused by thermal expansion, chemical or microstructural transformation or plastic deformation. A common classification is to distinguish between first, second and third order residual stresses whose occurrence is due to the heterogeneous

structure of materials. First order residual stresses (σ^I) are also called macroscopic residual stresses, because they are averaged over several crystallites. Second order residual stresses (σ^{II}) act on a smaller area, approximately between 0.01 - 1 mm. Third order residual stresses (σ^{III}) are called microscopic residual stresses because they act between atomic areas of the size between $10^{-6} - 10^{-2}$ mm. For the analysis of welding residual stress distributions, it is sufficient to examine only macroscopic or first order residual stresses.

2.2.1 Welding residual stresses

The weld zone experiences high temperature differences compared to the surrounding area during the welding process. Under the thermal load, the material expands and is restrained by the cooler surrounding material, which provokes stresses. Since the yield strength decreases as the temperature increases, these stresses often exceed the yield limit and provoke plastic strains. When plasticity occurs, existing residual stresses are relieved. This is the reason why, the initial residual stresses near the weld zone do not have any influence on the final residual stresses. On the contrary, the initial residual stresses in the parts located further away are usually not affected by welding.

The distribution of welding residual stress is very complex as it depends on several factors:

- structural dimensions
- material properties
- heat input
- number of weld passes
- welding sequence
- restraint conditions

Hence, it is difficult to predict the distribution of residual stress due to the welding operation. In this work, the influence of the mechanical material properties and the number of weld passes on the resulting residual stresses are studied.

For butt-welded tubes, a cylindrical coordinate system is applied to distinguish between radial, hoop and axial stresses, compare Fig. 2.2. During the cooling process, the weld zone and its vicinities shrink, hence the tube's diameter in this zone becomes smaller and a bending moment is generated. This generally leads to tensile stress on the weld toe and compressive axial stress on the outside surface. The stress components in thickness direction are very small and therefore not studied in this work.

2.3 Material properties

For a realistic welding simulation it is important to properly describe the temperature dependent material behavior. In this work, a bilinear elastic-plastic material model was chosen and therefore the Young's modulus and the yield strength as functions of the temperature are required to define the stress-strain curves. Richter [37] conducted tests for different steel types, but only for temperatures below 600°C. Furthermore, these results can only serve to show tendencies in the high temperature behavior. They cannot be adapted for the today's steel types.

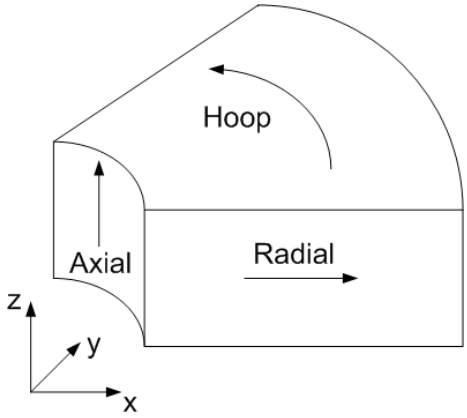

Figure 2.2: Stress definition in cylindrical coordinates

Especially for high strength steel, there are very few publications about the material behavior at different temperatures. Wichers' [47] doctoral thesis includes thermal as well as mechanical material data of the structural steel S355J2G3 for temperatures up to 1200°C. The only experiments with specimens made of S690 known to the author were conducted by Outinen [29] who measured the mechanical properties of S355 as well as S690 at high temperatures. The material data in the Eurocode 3, Part 1-2 [11] applies to various types of steel and was recently extended to include high strength steel. The thermal material properties published in the above mentioned sources are compared in chapter 4. The mechanical properties are discussed and compared to the test results in chapter 3.

2.4 Numerical simulation

A finite-element-simulation of the welding process is an acknowledged method to predict the welding residual stress distribution. Many simplifications still have to be made which lead to a decreased accuracy of the model. A major advantage of welding simulation is that the different welding parameters can be varied and thus their influence can easier be studied compared to experimental investigations. Furthermore, predictions about residual stress development during the welding process can only be made by using numerical simulation.

The description of the welding process is very complex and needs to be simplified in order to be analysed numerically. A common procedure is the decoupling of the welding process according to Fig. 2.3.

The bold arrows show the dominant dependencies, whereas the dotted lines visualize the less important effects, that often are not considered in welding simulation. The temperature field has a major influence on both the residual stress field and on the microstructural state field, but the reverse effects can often be neglected. For the realistic calculation of the stress field, the volume change due to microstructural phase transformation has to be considered as well the dependency of mechanical material behavior on the properties of the occuring chemical phases. The linking between the different aspects of welding simulation has been carefully studied in the past. Therefore, some links between the fields can be omitted to simplify the simulation and save computation time. In this work, the thermal and mechanical analysis are only sequentially coupled, so the heat effect of the plastic deformation in the mechanical field is neglected during the thermal analysis. This is the reason why, first a thermal analysis can be conducted to calculate the transient temperature field that is used

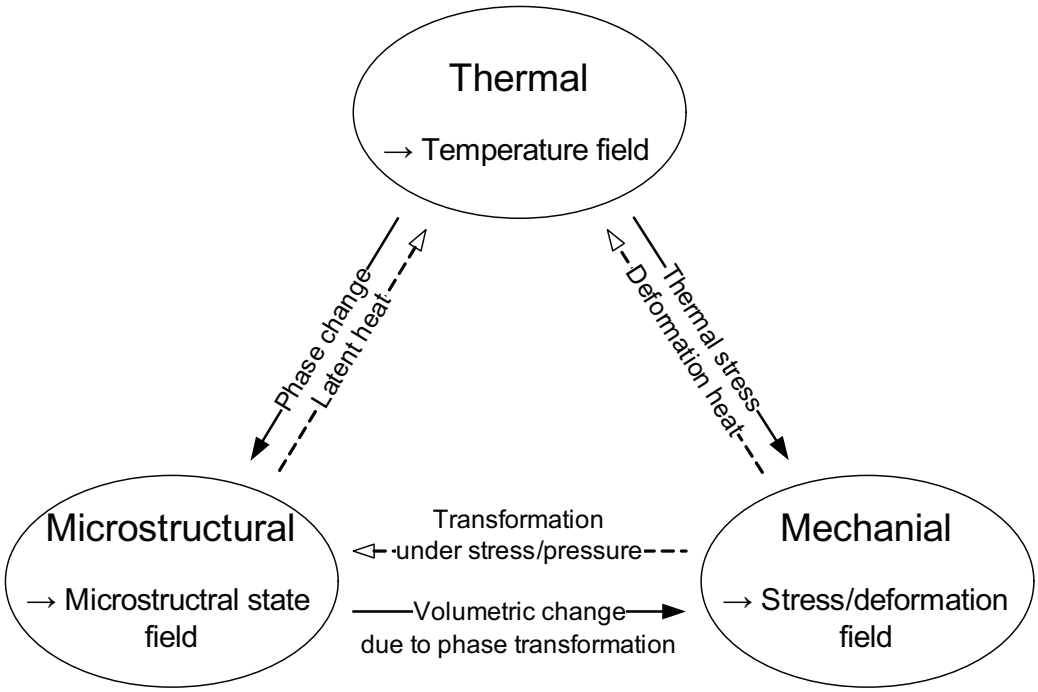

Figure 2.3: Decoupling and mutual coupling effects during welding

as input data for the second step. The material properties are considered to be temperature dependent but microstructural phase transformation is not considered in order to simplify the analysis.

The anaylsis is conducted with the finite element program ABAQUS and can be divided in four aspects:

- Simplifications
- Preprocessing
- Solution
- Postprocessing

2.4.1 Thermal modeling and simulation

The calculation of the thermal field is the basis in order to find the definition of the welding residual stress distribution. An analytical solution of the heat conduction problem exists only for simplified heat input and temperature independent material properties [33]. The first numerical welding simulations approximated the geometry using a two-dimensional model. This assumes axisymmetry for the butt-welding of tubes and neglects the influence of the weld start and end position. With the today's more powerful computational resources it is possible to realise three dimensional models. Still, concessions have to be made regarding the mesh density. Residual stress predictions not only require a dense mesh close to the heat source but also in the heat affected zone. Therefore, axi-symmetric models can be efficient.

In this work the base and the filler metal are identical and several phenomena such as convection and fluid motion in the weld pool are neglected during the thermal analysis. In

the single-pass models, the weld geometry is determined by the isothermal curves that exceed the melting temperature of the material and thus the weld is not directly modeled.

For the multi-pass models, the *model change option* in ABAQUS is used to simulate the deposition of the filler material. Lindgren [23] called this approach, the *quiet element technique*. With the model change option, the elements of the next weld pass are activated all at once after the completion of the previous weld pass. To activate the elements means to assign them realistic material properties. Deactivated elements are not actually removed from the model, but assigned zero valued material properties. In the heat flow model, the conductivity is therefore set to zero whereas in the mechanical analysis the stiffness is assumed to be zero. When activating the elements for the models in this work, they are added as strain free elements. The technique, that does not activate the elements of an entire weld pass, but that activates the elements when the filler material is actually deposited, is the so called *element birth technique*. This approach is more realistic, but it also complicates the analysis and is more time consuming.

2.4.2 Simulation programs

In this work, the finite element program ABAQUS was used to simulate the welding procedure and calculate the residual stress field. ABAQUS/CAE provides a coherent graphical interface, that is very helpful to create the geometry and the mesh. For more specific changes on the model, an input file can be created and afterwards modified. The heat input is modeled by the user subroutine DFLUX that is written as FORTRAN code. Temperature dependent material behavior can be realised without programming a user subroutine and a user-specified material model can be implemented with the subroutine UMATH. It is possible to model the welding analysis with ABAQUS as a coupled thermal-stress analysis. ABAQUS also provides an interface to model two-dimensional welding simulations that faciliates the setup of the model.

Another software that is used in many other works to model a welding procedure is ANSYS. A major advantage compared to ABAQUS is the ANSYS element birth and death procedure to simulate the filler material deposition. Volz [46] developed a macro to simulate the temperature dependent material behavior of structural steel. Together with other research institutions, CADFEM designed the welding simulation tool SST that can be used in combination with ANSYS to faciliate the modeling of the complicated processes during welding such as microstructural transformations and the heat source.

Furthermore, welding can be simulated with the software SYSWELD, that is also based on the finite element method. The analysis is divided into a thermo-microstructural and a mechanical part. SYSWELD allows a more realistic simulation of the material behavior by modelling it as a composition of different microstructures. Therefore, transformation effects as strains and plasticity can be taken into consideration. The downside of this software is that a large number of material data are needed. To avoid the costly and time consuming determination of these data sets, values are often extrapolated which decreases the accuracy of the material model and therefore the advantage of SYSWELD . Secondly, high computation times are required that restrict the density of the mesh [42]. The geometry and the mesh can either be generated with SYSWELD or be imported.

Chapter 3

Experiments

In numerical welding simulations not only input data of the geometry, the heat source, and the boundary conditions must be known but also the temperature dependent material behavior. In order to model the welding process as realistically as possible, it is fundamental to use accurate values for the thermal and mechanical material model. The experiments in this work aimed to verify the temperature dependent reduction factors for the yield stress and the Young's modulus given in the Eurocode 3 [11]. The yield stress and Young's modulus are used to define an ideal elastic-plastic material model and they can be deduced from the stress-strain curve. In order to find the deformational behavior and hence the stress-strain curves, a tensile testing is conducted. Therefore, specimens made of two different structural steels, S355 and S690, were tested at three different temperatures in a tensile test.

3.1 Specimen geometry

To faciliate the comparability to earlier test results, the following relation is used to define the proportion between the initial gage length L_0 and the initial cross section S_0:

$$L_0 = k \cdot \sqrt{S_0} \tag{3.1}$$

The international default value for k is 5.65, which results from the conversion of a round specimen to a rectangular form. For round specimens with the initial diameter d_0, the simplified relation 3.2 can be used [14].

$$L_0 = 5 \cdot d_0 \tag{3.2}$$

The tests in this work where conducted with round specimens made of two different structural steels, S355 and S690, with the geometry shown in Fig. 3.1. A round form was chosen in order to obtain a uniform temperature distribution. The aim was also to use the smallest diameter as possible so that the specimen heats up fast to save energy. Even though the code proposes also smaller specimen it is also noted that it is not advised to experiment with smaller specimen because it requires greater skill in testing.

The gage section has to be the smallest section, to provoke the failure to occur in this area. The outer part of the specimen is the so called shoulder, where the specimen is gripped by the machine. The specimens were taken out of the tubes that were used for the numerical models in chapter 5.

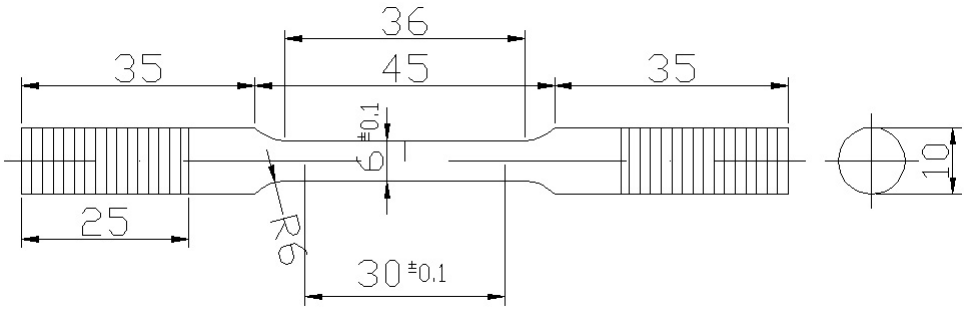

Figure 3.1: Specimen geometry according to the ASTM E8M-09 [40]

3.2 Performance of the tests

The tests were conducted at three different temperatures, namely room temperature, 250°C and 800°C. The temperatures 250°C and 800°C were chosen according to the above mentioned thesis by Wichers [47]. Using his results for specimens made of S355J2G3 to trace the Young's modulus as a function of temperature, one can observe a transition of behavior at the above mentioned temperatures. Furthermore, choosing 800°C as the highest testing temperature seems to be sufficient. It was stated in the doctoral thesis by Barsoum [2] on residual stress analysis for welded steel structures that this temperature is used as a cut-off-temperature in the finite element model, because the yield limit is disappearing in the high temperature range, so that no residual stresses are developed. Therefore the material properties in the high temperature range are assumed to be the same as at a fixed cut-off temperature. In general, the cut-off temperature is chosen to be half of the melting temperature:

$$T_{cut-off} = 0.5 \cdot T_{melt} \, (\cong 700°C) \tag{3.3}$$

It was chosen to conduct the tests at 800°C instead of 700°C because at around 700°C a phase transformation takes place, that was not desired for the study to be captured.

The deformational behavior of steel at elevated temperatures is dependent on the deformation rate. The American code for elevated temperature tensile tests, the ASTM E21-09 [39], indicates a strain rate of $0.005\,\mathrm{min}^{-1}$. The corresponding European code EN 10002-5 [14] suggests a strain rate in the range of 0.001 and $0.005\,\mathrm{min}^{-1}$ for the yield stress determination. After having exited the elastic zone the strain rate can be augmented. In order to use values, that are realistic for a welding procedure, the strain rates were derived from a cooling curve after welding. Therefore, a significant point within the weld in a model of a welded tubular K-joint was chosen and the temperature development during cooling analyzed [1]. The strain rate was then calculated by multiplying the thermal expansion factor α with the first derivative with respect to the time:

$$v = \alpha \frac{dT}{dt} \tag{3.4}$$

The values for the thermal expansion coefficient were taken from Wichers [47]. Because of the big impact of the strain rate on the test results, it was chosen to raise the strain rate during the experiments on the one hand to capture the effect on the stress-strain curve and, on the other hand, to save energy.

In order to minimize the influence of scatter due to the material properties or geometric defaults, for each temperature either two or three tests were chosen to be conducted with the same strain rate. For the tests at room temperature the strain rates were chosen according to the codes, because the deformational behavior is not strain rate dependent. It was decided to only conduct two tests at room temperature, because there are many other test results available. By using the relation 3.4 a strain rate of $0.002\,\mathrm{min}^{-1}$ was calculated for the tests at 250°C. Since this strain rate is within the range that the European code indicates, it was chosen to conduct three tests with this strain rate and to augment the strain rate by a factor of ten after the elastic zone has been captured. For the tests at 800°C, the cooling occurs faster than for the lower temperatures which is why a faster strain rate of $0.05\,\mathrm{min}^{-1}$ was calculated. As this is out of the range of the strain rates given by the codes, it was decided to conduct four tests at 800°C, whereof two tests use the strain rate of the code for the elastic zone and a strain rate ten times faster for the plastic zone. The second pair of tests uses the faster strain rate during the entire tests. As a conclusion, the four stress-strain curves should match in the plastic zone, where they were all conducted with the same strain rate.

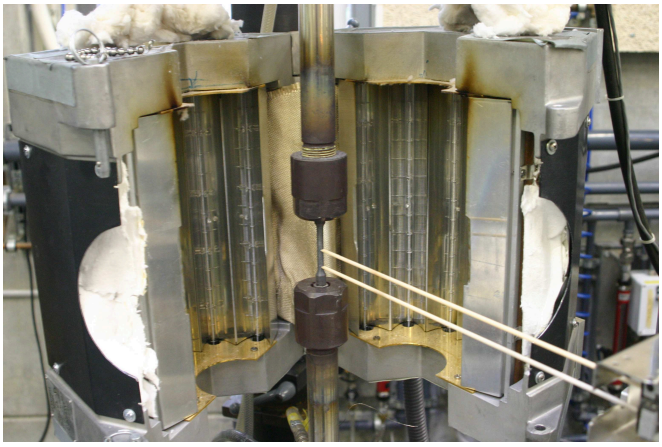

Figure 3.2: Test set-up

The tensile tests were conducted on a machine produced by Mohr & Federhaff AG (MFL) (Fig. 3.2). Before the specimen was installed into the machine, all the grips had to be carefully greased with a high temperature resistant grease. After the placement of the specimen, the thermocouple was inserted into a nut around the specimen (Fig. 3.3, to measure the temperature during the test. This temperature measurement set-up, was calibrated prior to the tests using a drilled specimen to compare the temperatures within the gage length to the temperature measured in the nut. With a stabilisation time of 5 minutes before the test it was assured, that the temperature would vary no more than 3°C within the gauge length during the test.

The deformation was evaluated with an extensometer (Fig. 3.3) that measured the rotation of two arms that were placed on the specimen. The initial distance between the two arms were 15 mm. After the oven was closed and insulated, the specimen was heated by radiation, which can result in a very fast heating process. Therefore, it had to be taken care that the temperature did not overshoot for the tests at 250°C. During the heating process, the machine had to work on load control. Otherwise, the specimen would have been under compression and possibly have buckled. After the temperature distribution was stable, the test was started on deformation control. It was not possible to control the test and measure the deformation

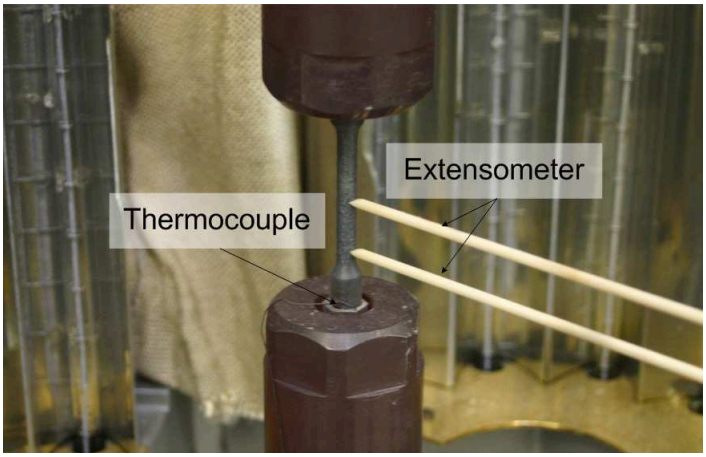

Figure 3.3: Specimen with thermocouple and extensometer

during the test with the same extensometer. Therefore, the deformation rate was measured on the bottom of the machine, which made it difficult to run the test at a precise strain rate. The resulting test matrices are shown in table 3.1 and 3.2

Temperature	**Test number**	**Strain rate [min^{-1}]**	
		1st strain rate	**2nd strain rate**
20°C	1	0.0005	0.02
250°C	2	0.004	-
	3	0.006	0.06
800°C	4	0.006	0.04
	5 and 6	0.05	-

Table 3.1: Test matrix for S355

Temperature	**Test number**	**Strain rate [min^{-1}]**	
		1st strain rate	**2nd strain rate**
20°C	1	0.001	0.02
	2	0.004	0.06
250°C	3	0.003	0.13
	4	0.002	0.35
	5	0.002	0.01
800°C	6 and 7	0.004	0.05
	8 and 9	0.05	-

Table 3.2: Test matrix for S690

3.3 Results

3.3.1 Steel type S355

The stress-strain curves for the tests with the steel type S355 are shown in Fig. 3.4.

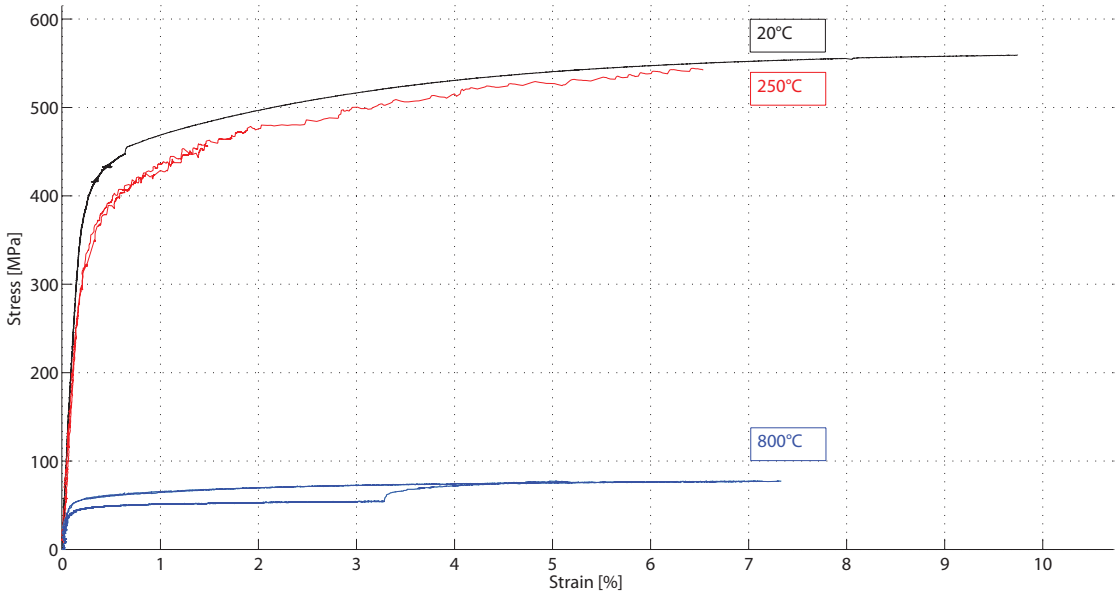

Figure 3.4: Stress-Strain curves of tests with S355

Test 2 at 250°C ended before the strain rate could have been augmented, because the extensometer slipped on the specimen. However, the test was sufficiently long to capture the yield stress. For the tests at 800°C, two different strain rates were used in principle. For the test 4, the elastic zone was captured by using approximately the strain rate given by the ASTM E21-09 [39]. At about 3%-strain, the strain rate was augmented to the value calculated with 3.4. During tests 5 and 6 the strain rate was maintained at the same value as for the second part in test 4. As it can be seen, the three curves are in very good agreement in the plastic zone, where the tests were run with approximately the same strain rate.

Temperature	**Test number**	**Young's modulus [GPa]**	$\mathbf{R_{P0.2}}$ **[MPa]**	$\mathbf{R_{P2.0}}$ **[MPa]**
20°C	1	205.2	428.9	
250°C	2	171.3	378.4	-
	3	182.2	381.5	476.6
800°C	4	41.3	47.7	52.9
	5	33.8	60.27	69.7
	6	44.8	58.73	69.9

Table 3.3: Summary of the results for the tests with S355

The Young's modulus was evaluated as tangent modulus in the elastic zone. The yield strength was determined at an offset of 0.2 % as described in the ASTM E21-09 [39]. For the elevated temperatures it was also evaluated at an offset of 2 %. The obtained values for the Young's modulus and the yield stress are listed in Table 3.3.

The values obtained by the tests were compared to the reduction factors given by the Eurocode 3 for fire design of steel structures [11] as well as the values found by Wichers [47]. Fig. 3.5 shows this comparison for the Young's modulus. In Fig. 3.6, the reduction factors for the yield strength were calculated with the values at an offset of 0.2 % strain and additionally

compared to the results by Outinen [29].

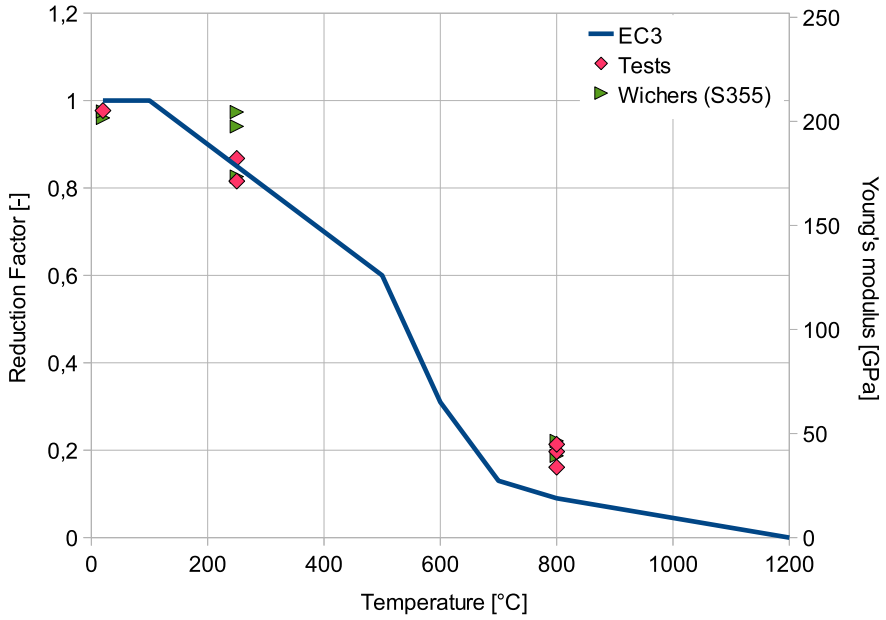

Figure 3.5: Young's modulus for S355 given by the EC3 [11], the test results and by Wichers [47]

The Young's modulus is difficult to determine especially in the high temperature range. For the tests at 800°C, the results are in very good agreement with the values found by Wichers [47]. The difference to the values given by the EC3 is higher than for the lower temperatures.

The values found for the yield strength are also in good agreement with the results published by Wichers [47]. The offset from the graph given in the EC3 [11] is smaller for 800°C than for 20°C and 250°C. The values found by Outinen [29] are remarkably higher than the rest of the curves.

3.3.2 Steel type S690

The stress-strain curves for the tests with the steel type S690 are shown in Fig. 3.7.

It can be observed that the specimens at 250°C are less temperature dependent than the tests at 800°C. Even if the strain rate is augmented by a factor higher than 100, this only results in a short elevation in the stress-strain curve. Whereas, the curves at 800°C show a clear temperature dependency. For the first two tests at 800°C the strain rate was augmented by a factor 10 after about 2 % strain and this second strain rate was used for the following two tests. Fig. 3.7 shows, that the four curves converge when the same strain rate is used. The obtained values for the Young's modulus and the yield stress at an offset of 0.2 % and 2 % are listed in Table 3.4.

Fig. 3.8 shows the comparison between the temperature dependency of the Young's modulus given by the Eurocode 3 [11], the test results and Outinen [29].

The Young's modulus for the test with the steel S690 is in very good agreement with the values given by the EC3. At 800°C, the results published by Outinen [29] are approximately three times as high as the values found in the tests. The test results for the yield strength are shown in Fig. 3.9 compared to the values given by the EC3 and found by Outinen [29].

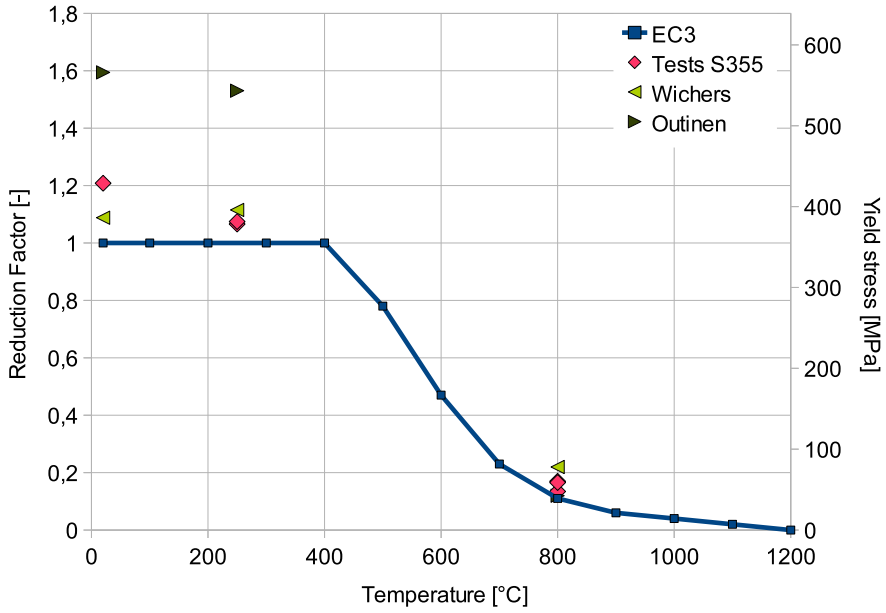

Figure 3.6: Yield strength for S355 given by the EC3, the test results, by Wichers [47] and by Outinen [29]

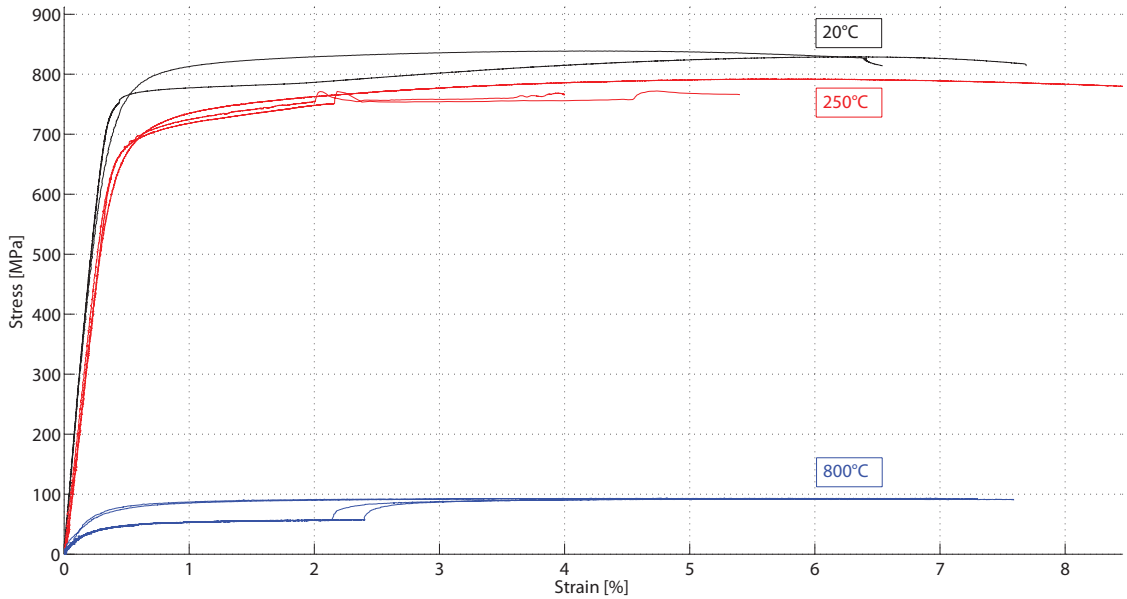

Figure 3.7: Stress-Strain curves of tests with S690

Temperature	Test number	Young's modulus [GPa]	$R_{P0.2}$ [MPa]	$R_{P2.0}$ [MPa]
20°C	1	216.3	768	
	2	213.3	775.1	
250°C	3	188.8	690.6	753.4
	4	183.5	689.1	748.1
	5	180.6	691.1	762.7
800°C	6	22.0	44.6	56.3
	7	22.3	45.5	56.5
	8	28.2	79.0	91.2
	9	24.9	76.5	89.8

Table 3.4: Summary of the results for the tests with S690

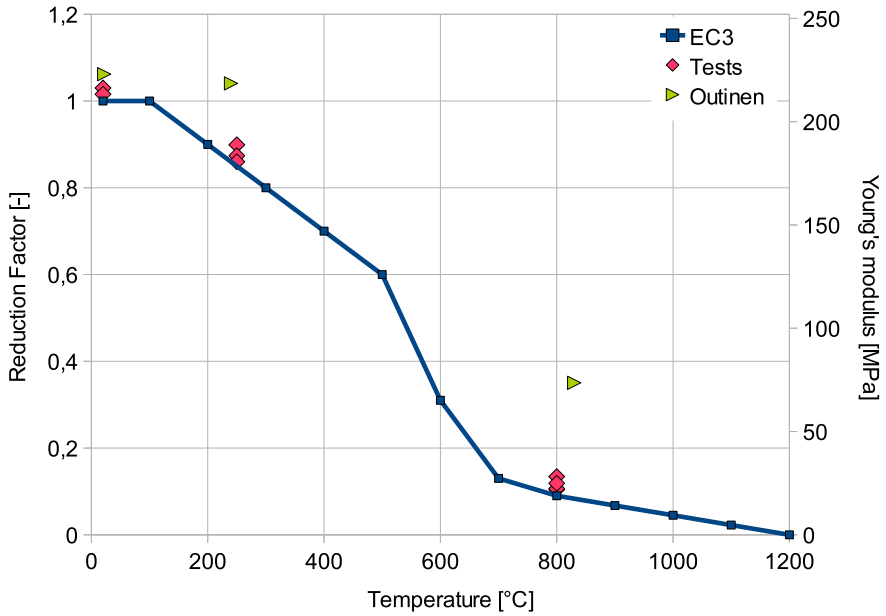

Figure 3.8: Young's modulus for S690 given by the EC3 [11], the test results and by Outinen [29]

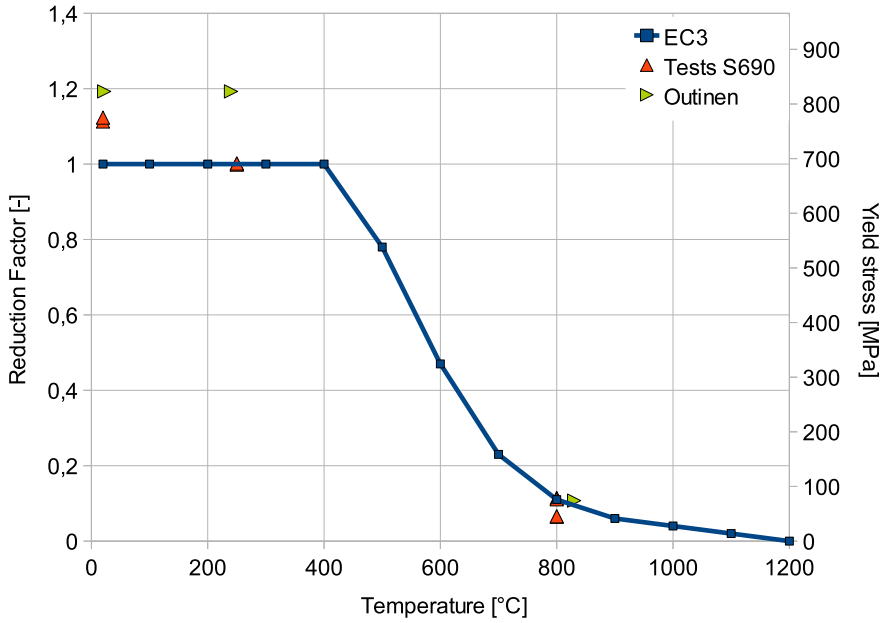

Figure 3.9: Yield strength for S690 given by the EC3, the test results and by Outinen [29]

For both steel types, the yield strength at 250°C already demonstrates a decrease of about 10 % compared to the value at 20°C, which is not considered by the Eurocode 3. The more important change occurs though between 250°C and 800°C. This seems to be even more important for the S690. To verify applicability of the curves given in the EC3 for high strength steel, more tests at different temperatures seem necessary.

Chapter 4

Numerical simulation

4.1 Thermal analysis

4.1.1 Theory

The fundamental principles for the field equation of heat conduction are the Conservation of Energy and the Fourier's law. By definition temperature is a time dependent scalar field:

$$T = T\left(x, y, z, t\right) \tag{4.1}$$

The conjugate thermodynamic quantity is the heat flux density $\mathbf{q}$, which defines the heat flux per area.

$$\mathbf{q} = \left[q_x, q_y, q_z\right]^T \tag{4.2}$$

Fouriers law of heat conduction states that the heat flow $\mathbf{q}$ is proportional to the negative temperature gradient generated by a temperature difference (heat flows from high to low temperature zones). With the assumption that steel is a homogenous and isotropic material this can be written as follows:

$$\mathbf{q} = -\lambda\, \mathbf{grad}\left(T\right) \tag{4.3}$$

The conservation of energy for a small volume element is shown in Fig. 4.1 where q_x, q_y, q_z are the projection of the heat flux densities on the normal of the surfaces surrounding the volume. According to the ABAQUS manual [41] the conservation of energy in an integral form can be written as:

$$\int_V \rho\, \dot{U}\; dV = \int_V r\; dV + \int_S \mathbf{q} \cdot \mathbf{n}\; dS = \int_V r\; dV + \int_V div\left(\mathbf{q}\right)\; dV \tag{4.4}$$

where ρ is the density of the material, $\dot{U}$ is the material time rate of the internal energy and r is the heat supplied externally into the body per unit volume. It is assumed that thermal and material problems are uncoupled in a sense that U depends only on the temperature and that $\mathbf{q}$ and r do not depend on stress or strain rates. This is due to the fact that the heat produced by the deformation of the material is negligible compared to the heat input of the welding arc. This fact is usually expressed by introducing a specific heat capacity

$$c\left(T\right) = \frac{\partial U}{\partial T} \tag{4.5}$$

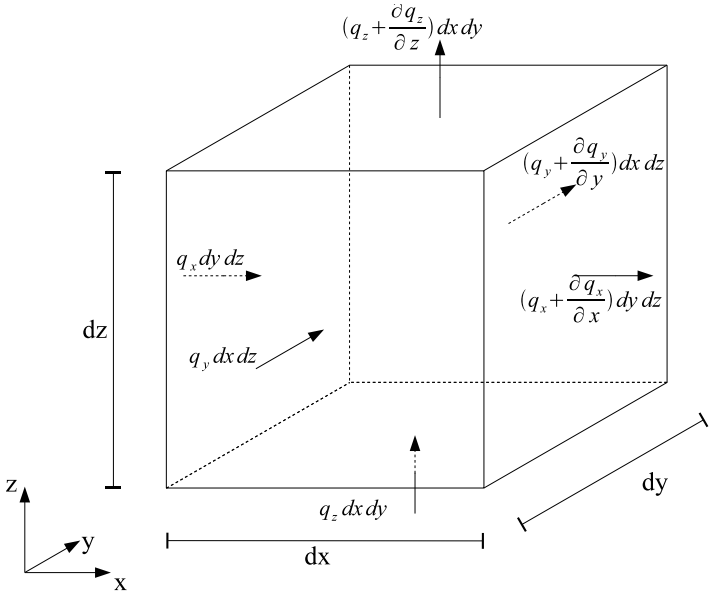

Figure 4.1: Heat fluxes on a volume element

which can be transformed into

$$\dot{U} = \frac{\partial U}{\partial t} = \frac{\partial U}{\partial T} \cdot \frac{\partial T}{\partial t} = c(T)\frac{\partial T}{\partial t} \tag{4.6}$$

Finally this leads to the equation

$$\lambda\, div\left[(grad)\,(T)\right] + r = \lambda\left[\frac{\partial^2 T}{\partial x^2} + \frac{\partial^2 T}{\partial y^2} + \frac{\partial^2 T}{\partial z^2}\right] + r = c\,\rho\,\frac{\partial T}{\partial t} \tag{4.7}$$

In order to solve this equation initial and boundary conditions have to be defined. The initial condition is the temperature distribution at the time t=0 for the entire body:

$$T(x, y, z, t = 0) = T_0(x, y, z) \tag{4.8}$$

The boundary conditions specify the temperature distribution on the surfaces of the body. Three types of boundary conditions can be described.

The Dirichlet or first-type boundary condition

$$T(x, y, z, t) = T^S(x, y, z, t) \text{ on } \mathrm{S}_1 \tag{4.9}$$

where $T^S(x, y, z, t)$ is the prescribed temperature at specific points and surfaces of the body.

The Neumann or second-type boundary condition

$$q_n^S = -\lambda\frac{\partial T}{\partial n} \text{ on } \mathrm{S}_2 \tag{4.10}$$

4.10 describes the heat flux density normal to a surface as a function of position and time. The index n stands for the direction of the unit normal vector.

The Robin or third-type boundary condition The Robin boundary conditions describes the heat transfer to the surrounding medium by

$$q_n^S = h\,(T - T_0) \text{ on } \mathrm{S}_3 \tag{4.11}$$

where h is the heat transfer coefficient and T_0 is the gas or liquid temperature of the surrounding medium. In this boundary condition, the heat transfer is proportional to the temperature difference between the surface and the ambiance and includes convection and radiation. The heat transfer coefficient h can be temperature dependent.

Heat transfer by convection Heat transfer by convection occurs in liquids or gases caused by movement of molecules. It can be distinguished between natural and forced convection. Natural convection can only occur in a gravity field because the movement is due to the differences in density caused by temperature gradients. Forced convection is the result when external forces maintain the movement (e.g. a fan or the blow effect of the welding arc). The Newton's law describes convection with

$$q_c = h_c\,(T - T_0) \tag{4.12}$$

where h_c is the heat transfer coefficient due to convection. The heat transfer coefficient is dependent on the flow conditions, the surface and temperature differences between the material and the surroundings.

Heat transfer by radiation According to the Stephan-Boltzmann's law the heat flow density of a gray body caused by radiation is proportional to the forth power of the temperature differences to its surroundings:

$$q_r = \epsilon\sigma_0 \left(T^4 - T_0^4\right) \tag{4.13}$$

where ϵ is the emissivity and σ_0 is the Stefan-Boltzmann constant ($= 5.670 \cdot 10^{-8} W/m^2K^4$). The emissivity can be temperature dependent in the high temperature range. By linearizing equation 4.13 the heat flow density caused by radiation can be expressed in the same form as the heat flow density due to convection, so that both boundary conditions can be combined.

4.1.2 Finite Element solution

The analytical solution of equation 4.7 can only be obtained for simple geometries, boundary conditions and temperature independent material properties. That is why the use of a finite element procedure can be necessary. We start with what is called the Galerkin formulation by multiplying equation 4.7 with a virtual weighting function δT and integrating over the entire volume:

$$\int_S \delta T\,\lambda\,\mathbf{grad}\,(T)\cdot\mathbf{n}\,dS - \int_V \mathbf{grad}\,(T)\cdot\lambda\cdot\mathbf{grad}\,(\delta T)\,dV + \int_V r\,\delta T\,dV = \int_V c\,\rho\,\frac{\partial T}{\partial t}\,dV \tag{4.14}$$

Introducing the boundary conditions into equation 4.14 and using the Gauss theorem we get:

$$\int_V \mathbf{grad}\,(\delta T)\cdot\lambda\,\mathbf{grad}\,(T)\,dV + \int_V \delta T\rho c\frac{\partial T}{\partial t}dV = \int_V \delta T\,r\,dV + \int_S \delta T\,q\,dS \tag{4.15}$$

where the Q^i are concentrated heat flow inputs. The principle of virtual temperatures is used in the same way as the more common principle of virtual displacements, that is, in order to determine the unknown temperature field at its nodes. One major difference here in comparison to elastostatics is the presence of the time variable, which in general is treated separately. So the next step is to define the temperature field by separating the time and space dependency:

$$T = T(x, y, z, t) = \mathbf{N}(x, y, z) \cdot \mathbf{T}(t) \tag{4.16}$$

The same can be done for the virtual temperature field $\delta\mathbf{T}$. Here already the next step is included, which is to discretize the body and assume it to be a batch of so called finite elements. So the vector $\mathbf{T}(t)$ contains the temperature evolution at the nodes of the finite elements. In the matrix $\mathbf{N}$ the so called shape or interpolation functions are stored. The next step would be now to define properly the shape functions $\mathbf{N}_e$ at an element level, which will be omitted here (for the case of continuum elements it is referred here to the ABAQUS manual [41]). If the preceding formulations are inserted into 4.15 and the virtual energy is assembled over the whole body, the principle finite element equations in heat transfer analysis are obtained:

$$\mathbf{C}\dot{\mathbf{T}} + \left(\mathbf{K}^{\lambda} + \mathbf{K}^{conv} + \mathbf{K}^{rad}\right)\mathbf{T} = \mathbf{Q}^{inp} + \mathbf{Q}^{conv} + \mathbf{Q}^{rad} \tag{4.17}$$

where $\mathbf{C}$ is the heat capacity matrix,

$$\mathbf{C} = \sum_e \int_{V_e} \mathbf{N}_e^T \, \rho c \, \mathbf{N}_e \, dV \tag{4.18}$$

$\mathbf{K}^{\lambda}$ is the conductivity matrix,

$$\mathbf{K}^{\lambda} = \sum_e \int_{V_e} \mathbf{B}_e^T \, \lambda \, \mathbf{B}_e \, dV \tag{4.19}$$

$\mathbf{K}^{conv}$ is the convection matrix,

$$\mathbf{K}^{conv} = \sum_e \int_{S_{conv}} h_{conv} \, \mathbf{N}_e^T \mathbf{N}_e \, dS \tag{4.20}$$

and $\mathbf{K}^{rad}$ is the radiation matrix

$$\mathbf{K}^{rad} = \sum_e \int_{S_{rad}} h_{rad} \, \mathbf{N}_e^T \mathbf{N}_e dS \tag{4.21}$$

The vector of the heat flow input $\mathbf{Q}_{inp}$ is given by:

$$\mathbf{Q}^{inp} = \mathbf{Q}_B + \mathbf{Q}_S \tag{4.22}$$

where $\mathbf{Q}_B$ is a volumetric heat flow input

$$\mathbf{Q}_B = \sum_e \int_{V_e} \mathbf{N}_e^T \, r \, dV \tag{4.23}$$

and $\mathbf{Q}_S$ is a surface heat flow input

$$\mathbf{Q}_S = \sum_e \int_{S_e} \mathbf{N}^T q^S dS \tag{4.24}$$

The heat flows $\mathbf{Q}^{conv}$ and $\mathbf{Q}^{rad}$ in equation 4.17 are due to convection and radiation boundary conditions. For the temperature distribution of the surrounding medium the same interpolations as for the surface temperatures are used and for the radiation boundary condition the linearized form is used, which leads to:

$$\mathbf{Q}^{conv} = \sum_e \int_{S_{conv}} h_{conv}\, \mathbf{N}_e^T \cdot \mathbf{N}_e \cdot \mathbf{T}_0\, dS \tag{4.25}$$

$$\mathbf{Q}^{rad} = \sum_e \int_{S_{rad}} h_{rad}\, \mathbf{N}_e^T \cdot \mathbf{N}_e \cdot \mathbf{T}_0\, dS \tag{4.26}$$

By combining the conductivity, the convection, and the radiation matrix as well as the heat supply vectors 4.17 can be written as

$$\mathbf{C}\,\dot{\mathbf{T}} + \mathbf{K}\,\mathbf{T} = \mathbf{Q} \tag{4.27}$$

In order to numerically solve the semidiscrete heat equation, the time interval for the solution has to be divided into different increments. The equation system is therefore only evaluated at every discrete time $n \cdot \Delta t$. The most common algorithms to solve a parabolic problem as the heat transfer are the generalized trapezoidal methods.

4.1.3 Heat source

The complex process in the weld pool is simplified by neglecting material movement in the molten zone including heat transfer by convection and radiation. Therefore, the heat source model only describes the effect of the heat source. The principle parameter used in the heat source model is the heat quantity Q [J] in momentarily acting sources. The heat losses during the complex processes of welding are considered by the heat efficiency η_h and combine the losses by radiation of the weld arc, heat dissipation by convection and spray losses. The heat flow q [J/s] for continuously acting sources is the product of voltage U [V], amperage I [A] and heat efficiency:

$$q = \eta\, U I \tag{4.28}$$

The heat efficiency for gas metal arc welding is estimated in the range of 0.65 and 0.90. Another parameter, that has an important influence on the temperature field, is the welding speed that for gas metal arc welding usually lies below 15 mm/s [33]. The spatial distribution of the welding source can either be a point, a surface or a volume source. In general, surface and volume sources are preferred for the finite element model because they seem to be more realistic. Also, a surface and a volume source can be combined [21], where the surface heat input models the heat by the welding arc and the volumetric heat source simulates the heat input of the melt drops.

The most common heat source models use Gaussian normal distributions over a circular surface or a hemisphere (figure 4.2). Another approach to simulate the welding source is by prescribing temperatures as boundary conditions. For the models in this work either a hemispherical or a spherical volumetric heat source with uniform heat flux density is used.

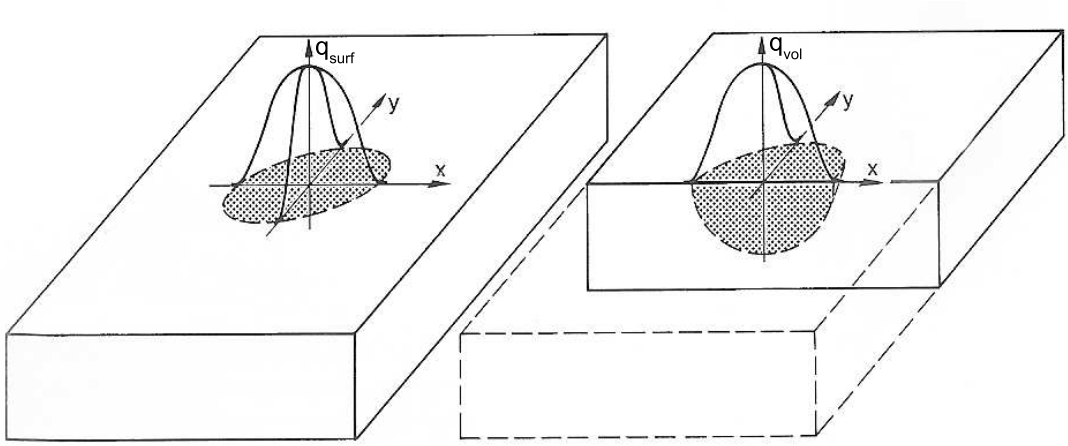

Figure 4.2: Welding heat sources with Gaussian distribution of the surface heat flux density q_{surf} and the volume heat flux density q_{vol} [35]

4.1.4 Thermal material properties

For the heat transfer analysis, temperature dependent curves for the thermal conductivity λ, the specific heat capacity c and the density ρ are needed. Richter [37] conducted many tests to obtain these material characteristics for different steel types, but only for temperatures up to 600°C. For the structural steel grade S355, values at high temperatures can be found in a work by Wichers [47]. There are no tests for structural high strength steel as S690 known to the author. The Eurocode 3 [11] provides temperature dependent values for the thermal conductivity and the specific heat capacity but without distinguishing between different steel types. The same material properties were used for the filler and the base metal.

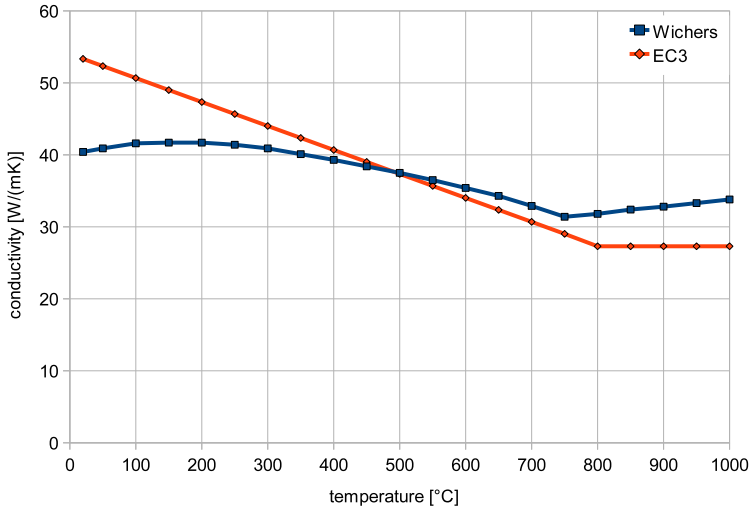

Figure 4.3: Thermal conductivity λ according to EC3 and Wichers [47]

Thermal conductivity Fig. 4.3 presents the thermal conductivity given in the Eurocode compared to the values found by Wichers [47]. For the ABAQUS models in this work the data

from the EC 3 is used. For temperatures above the melting temperature, the conductivity is multiplied by three to account for heat transfer by convection in the weld pool. Wichers [47] calculated the thermal conductivity from the values obtained for the electric resistance by using the Wiedemann Franz law.

Specific heat capacity During phase transformations, the material loses or accumulates energy without changing its temperature. To capture this so called latent heat in a numerical simulation, either the specific heat can show a significant maximum at phase transformation temperatures or a latent heat has to be considered. Therefore, the Eurocode uses a significant maximum for the α-γ-transformation at 735°C. To account for the solid-liquid phase change, a latent heat of 247000 J/kg is used in the ABAQUS models in this work refering to Raymond and Chipman [36]. Fig. 4.4 shows that Wichers [47] considered a lower maximum for the specific heat than the Eurocode.

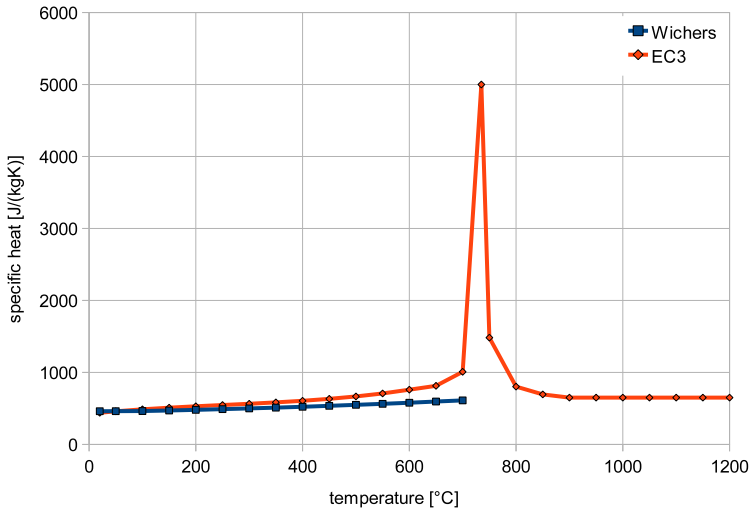

Figure 4.4: Specific heat c according to EC3 and Wichers [47]

Density The density can be calculated by using the relation with the coefficient of thermal expansion, that is given in Chapter 4.2.2. This is the reason why, Wichers [47] finds a discontinuity point at the temperature where phase transformation occurs. The Eurocode specifies a constant density. Richter [37] proposes to use a linear approach for the density between termperatures from 0 to 1000°C, which is in good agreement with the values found by Wichers [47]. For the thermal analysis in the ABAQUS models, the constant density from the Eurocode was considered.

4.1.5 Boundary conditions

Convection and radiation are considered for modeling boundary heat transfer. The values were taken from Brown and Song [5] who assumed that the film coefficient for convective heat transfer is dependent on temperature and orientation of the boundary. By using the linearized

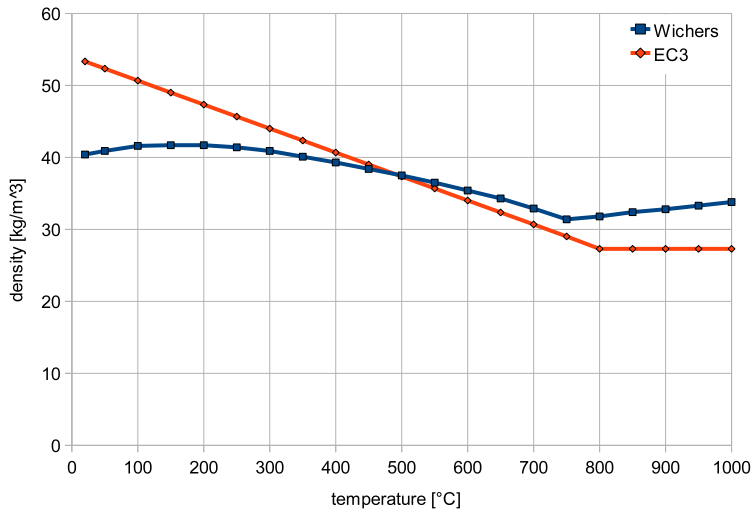

Figure 4.5: Density ρ according to EC3 and Wichers [47]

form for radiation, both boundary conditions were combined:

$$\begin{aligned} h_{total} &= h_{conv} + h_{rad} \\ h_{rad} &= \epsilon\sigma \left(T^3 + T^2 T_0 + T T_0^2 + T_0^3\right) \end{aligned} \tag{4.29}$$

where σ is the Stefan-Boltzmann constant and T_0 is the reference sink temperature value. It was assumed that radiation occurs only from the surface to the ambient air and not between surfaces. So, no radiation on the inside of the tubes was considered.

At low temperatures, the heat flow by convection and radiation is small compared to the heat transfer by conduction. This is why, the thermal boundary conditions were only applied on the outer surface of the tubes close to the weld in order to save computation time.

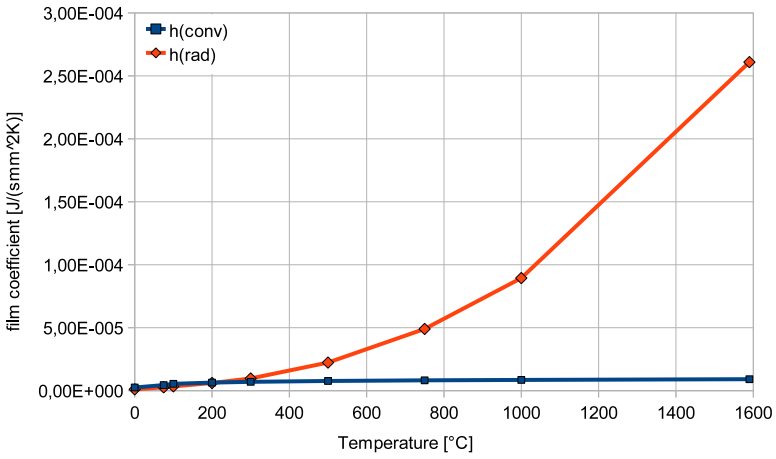

Figure 4.6: Film coefficient due to convection h_{conv} and due to radiation h_{rad} according to Brown and Song [5]

4.2 Mechanical analysis

4.2.1 Theory

As was mentioned above, the thermal and mechanical processes in this work were considered to be only sequentially coupled. Therefore, the thermal analysis is followed by a mechanical analysis where the nodal temperature histories calculated in the thermal analysis are used as input data to calculate the resulting strains during welding. The same finite element mesh is used as for the thermal analysis and linear brick elements with reduced integration are used with three degrees of freedom at each node.

The basis for classic finite elements in mechanics is the equilibrium formulation written as principle of virtual work:

$$\int_V \boldsymbol{\sigma} : \delta\boldsymbol{\varepsilon}\, dV = \int_S \delta\mathbf{n}^{\mathbf{T}} \cdot \boldsymbol{\sigma} \cdot \delta\mathbf{u}\, dS + \int_V \mathbf{f} \cdot \delta\mathbf{u}\, dV \tag{4.30}$$

where

$$\boldsymbol{\varepsilon} = \frac{1}{2}\left[\mathbf{grad}\,(\mathbf{u}) + \mathbf{grad}^T(\mathbf{u})\right] \tag{4.31}$$

is the linearised strain tensor derived from the displacement field, defining a linear operator on the displacement field. $\delta\mathbf{u}$ is a virtual displacement field and $\delta\varepsilon$ is the virtual strain derived by the strain operator from the virtual displacement field. Until now no hypothesis was made for the constitutive equations. The finite element solution is then implemented by interpolating $\mathbf{u}$ between a finite number of points, the nodes defining the finite element mesh:

$$\mathbf{u} = \mathbf{N}\,\mathbf{u_e} \tag{4.32}$$

For an exact description of the implementation of the specific elements reference is made to the ABAQUS manual [41].

In this work the chosen material model is an isotropic elasto-plasticity model which is often used for metals because of its simple form. When neglecting the strain components due to volumetric change during phase transformation, transformation plasticity and creeping, the total strain can be written as follows:

$$\boldsymbol{\varepsilon} = \boldsymbol{\varepsilon}_{el} + \boldsymbol{\varepsilon}_{pl} + \boldsymbol{\varepsilon}_{th} \tag{4.33}$$

where the components represent elastic, plastic and thermal strain respectively. The strain tensor, as every tensor of second order, can be decomposed in a volumetric and a deviatoric component:

$$\varepsilon_{vol} = trace\,(\boldsymbol{\varepsilon}) \tag{4.34}$$

and

$$\mathbf{e} = \boldsymbol{\varepsilon}_{dev} = \boldsymbol{\varepsilon} - \frac{1}{3}\varepsilon_{vol}\mathbf{I} \tag{4.35}$$

This procedure is valid for each component of the strain tensor. Additionally, the stress tensor $\boldsymbol{\sigma}$ can be decomposed in the same manner:

$$p = -\frac{1}{3}trace\,(\boldsymbol{\sigma}) \tag{4.36}$$

and

$$\mathbf{s} = \boldsymbol{\sigma} + p\mathbf{I} \tag{4.37}$$

With introducing the bulk and the shear modulus, that are computed using the temperature dependent Young's modulus $E(T)$ and Poisson's ratio $\nu(T)$ given by the user as input value:

$$K(T) = \frac{E(T)}{3(1-2\nu(T))} \tag{4.38}$$

$$G(T) = \frac{E(T)}{2(1+\nu(T))} \tag{4.39}$$

the elasticity law can be rewritten as follows:

$$p = -K(T)\varepsilon_{vol} \tag{4.40}$$

and

$$\mathbf{s} = 2G(T)\mathbf{e}^{el} \tag{4.41}$$

The transition from elastic to plastic behavior, where non-reversible deformations occur, is called yield. The plasticity model in this work is assumed to be rate independent and uses the von Mises yield criterion. The yield condition for the von Mises criterion is expressed as:

$$q - f_y = 0 \tag{4.42}$$

where

$$q = \sqrt{\frac{3}{2}\mathbf{s} : \mathbf{s}} \tag{4.43}$$

and f_y is the yield stress, that is dependent on the equivalent plastic strain $\bar{e}^{pl}$ and on the temperature ABAQUS. The flow rule assumes that yielding occurs in the direction normal to the yielding surface defined by the von Mises criteria:

$$d\mathbf{e}^{pl} = \bar{e}^{pl}\mathbf{n} \tag{4.44}$$

where

$$\mathbf{n} = \frac{\frac{3}{2}\mathbf{s}}{q} \tag{4.45}$$

Strain hardening was not considered in this work to simplify the analysis. The equations 4.42 to 4.45 describe the material behavior in an incremental form. For each increment at each point q is calculated and compared to the yield stress f_y. If this value is reached, plastic flowing occurs and the incremental equations are integrated by using the Euler backward method. The thermal strains are generated by the thermal expansion coefficients α shown in Fig. 4.8 according to the expression:

$$\boldsymbol{\varepsilon}_{th} = \alpha(T)(T - T_0))\,\mathbf{I} \tag{4.46}$$

where T_0 is the reference temperature.

4.2.2 Mechanical material properties

The mechanical material properties are considered to be temperature dependent, but there are very few experimental data for the material behavior at high temperatures of structural steel. Therefore, the reduction factors from the Eurocode 3, Part 1-2 were used for the bilinear elastic-plastic material model in ABAQUS. The temperature dependent values of the Young's modulus and the yield stress given by the Eurocode 3 are shown in Fig. 4.7. The Poisson's ratio is assumed to be a constant value of 0.3.

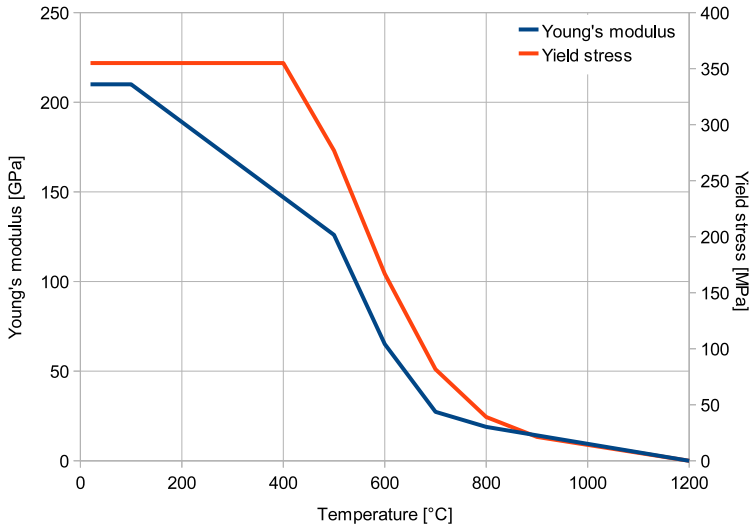

Figure 4.7: Young's modulus and Yield strength according to EC3

Thermal expansion factor The thermal expansion coefficient is needed to calculate the thermal dilatation due to a change of temperature. Fig. 4.8 shows the thermal expansion coefficient measured by Wichers [47] with three different devices and the values given in the Eurocode 3. It can be seen that the curve changes between 700 and 850°C. This is due to a change of microstructure and occurs for all the curves in the same temperature range. For the ABAQUS models, the thermal expansion coefficient from the Eurocode 3 were chosen.

Especially for the multi-pass model it is important to include an annealing function during the mechanical analysis to simulate the relaxation of plastic stresses and strains of the remelted material. This relaxation is due to different microstructural processes as recrystallization and rapid creep [28]. For the annealing function in ABAQUS, a temperature can be specified over which all plastic strains are set to zero. In this work, the melting temperatures is estimated to 1465°C and is also chosen for the annealing temperature.

4.2.3 Boundary conditions

The boundary conditions in the mechanical analysis are chosen to only prevent rigid body movement and are applied 200 mm away from the weld centerline. Fig. 4.9 shows the boundary conditions when the entire tube is modeled and Fig. 4.10 when only half of the tube in axial direction is modeled. For the model in Fig. 4.10 all the nodes at the weld center have to be constrained in axial direction as symetric boundary conditions whereas the far end from the weld has to be free to move axially but constrained in the other directions.

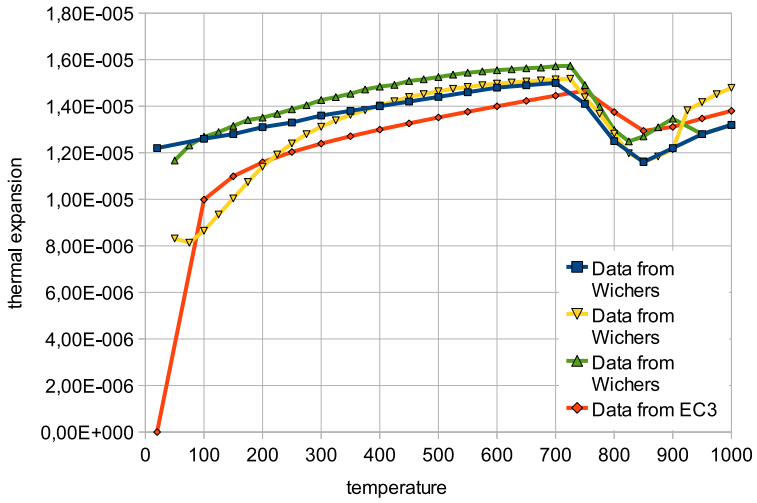

Figure 4.8: Thermal expansion coefficient according to Wichers [47] and EC3

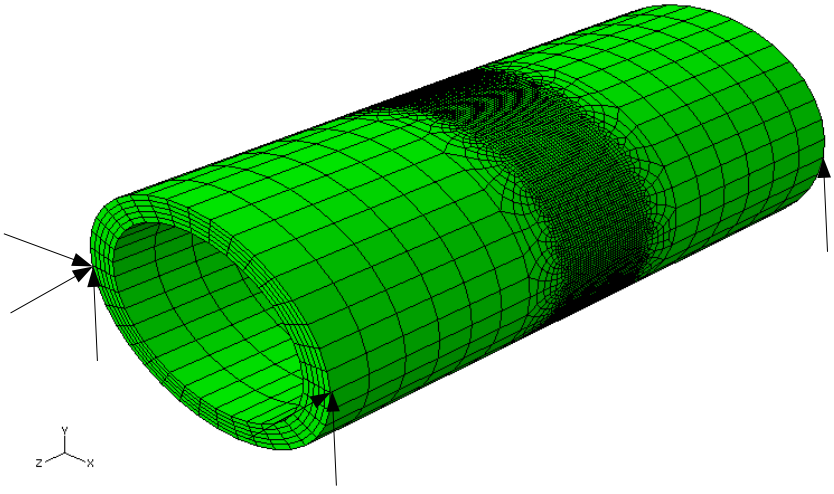

own

Figure 4.9: Mechanical boundary conditions for complete tube

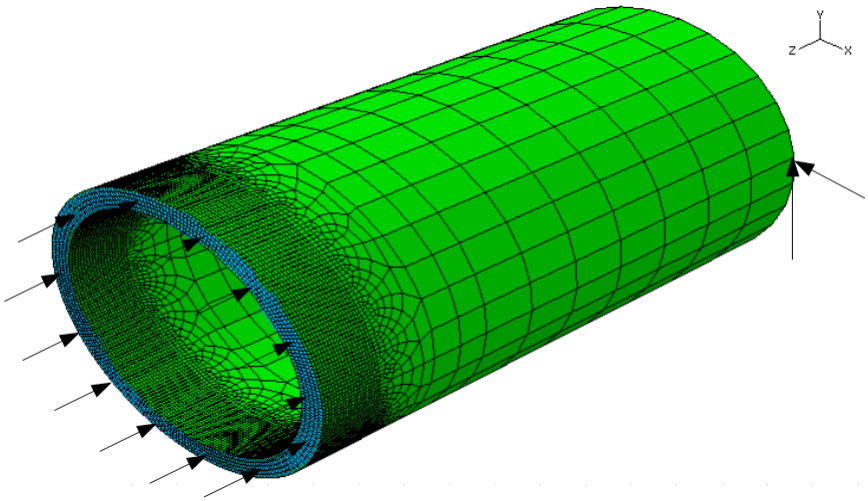

Figure 4.10: Mechanical boundary conditions for half tube

Chapter 5

Finite Element Models

All the models in this work are developed based on the ABAQUS software listed in Chapter 2.4.2. Only three-dimensional and no axisymmetric models were analysed. The steel types, S355 and S690, and dimensions are chosen according to a study at the EPFL (École Polytechnique Fédérale de Lausanne). It is assumed that the temperature field is not dependent on the stress or deplacement solution, so the analysis was conducted sequentially coupled. First the temperature distribution is calculated in a heat transfer analysis and then applied as a load during the mechanical analysis. The assumption made is that only small displacements occur during welding. The decoupling of the two analysis steps is an acknowledged simplification to save computation time.

Besides decoupling the analysis, various assumptions and simplifications were made in order to simulate the welding procedure in an efficient way. To verify the chosen modelling technique and to estimate the influence of the simplifications in this work, the model analysed in the publication by Karlsson and Josefson [19] is simulated.

5.1 Verification of the modelling technique

The wall thickness and outer diameter of the analysed pipe is 8 mm and 114.3 mm respectively. The idealized geometry of the weld is shown in Fig. 5.1 a. The material used is carbon-manganese steel which is why it is assumed to behave in a similiar way as the structural steel S355. The simulated welding procedure is MIG-welding.

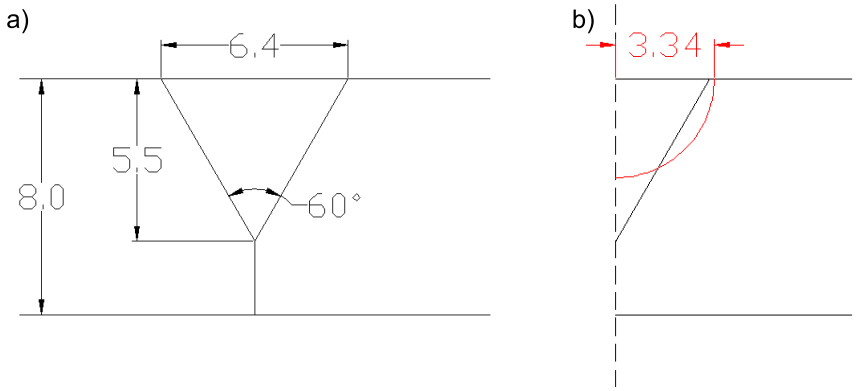

Figure 5.1: a) Weld geometry used in Karlsson and Josefson [19], b) Dimensions of the heat source in the model

In the publication the filler material was modeled. In this work it is assumed that base and filler metal are the same. The weld itself is not modeled, but the isothermal curves with temperatures above the melting point define the weld zone. The temperature dependent curves for the base metal material properties that are used in the verification model are taken from Karlsson and Josefson [19] and presented in Fig. 5.2 and 5.3. Note that the conductivity for temperatures above the melting point is multiplied by three to account for convection and stirring in the weld pool. The latent heat during solid liquid phase transformation was included with 272 kJ/kg Siddique [38].

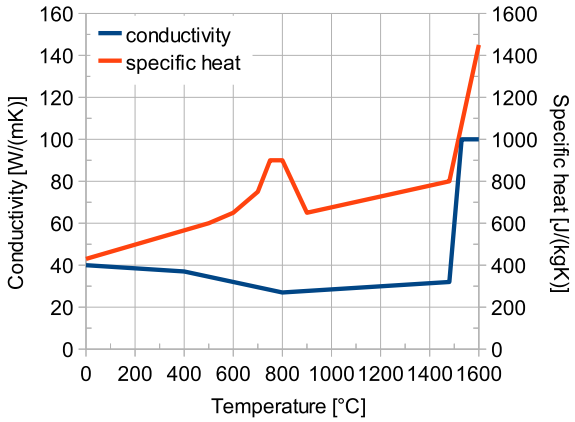

Figure 5.2: Thermal material data used in Karlsson and Josefson [19] for the base metal

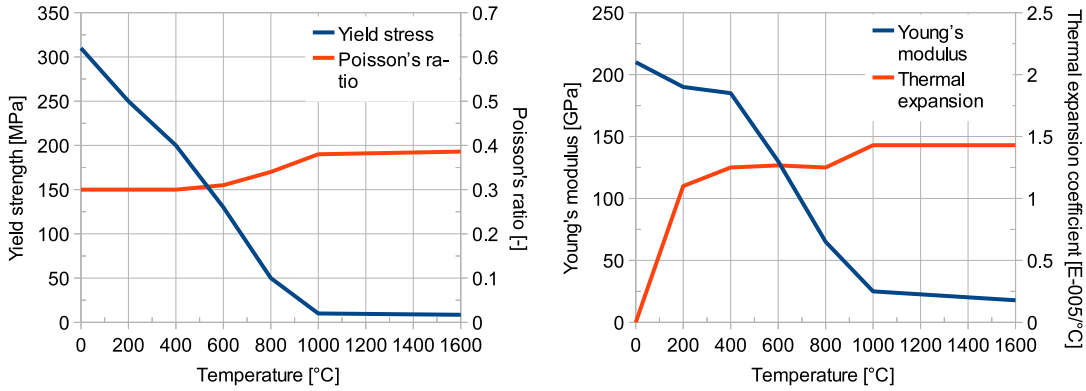

Figure 5.3: Mechanical material data used in Karlsson and Josefson [19] for the base metal

To save computation time and according to the model chosen by Karlsson and Josefson [19], only half of the pipe relative to the weld line is modeled. A dense mesh in the weld vicinity and the heat affected zone is realized. In the weld zone, the thickness is modeled by five elements whereas it descends to three elements over the thickness in the parts located further away. This leads to a number of almost 32000 elements for the entire model. The same mesh with linear continuum elements is used for the thermal and the mechanical analysis.

The heat input is modeled by a constantly moving quarter of a sphere with uniform heat density distribution and realized with the user subroutine DFLUX. The radius r of the corresponding sphere is calculated by assuming that the cross section of the weld is equal

to the section of a quarter circle with the radius r. For the verification model, this leads to $r = 3.34$ mm, compare 5.1 b. For the determination of the circular path of the welding source, the center point of the heat source runs on the outside of the tube on the weld center line. According to Karlsson and Josefson [19], the heat input for the symmetric model is 630 kJ/m and the welding arc is moving at 6.0 mm/s. As mentionend in chapter 4.1.3, the arc efficiency can only be approximated and here a value as high as 90 % was assumed.

During the thermal analysis radiation is neglected and only convective boundary conditions are considered. The temperature dependent curve of the convection coefficient is shown in Fig. 5.4.

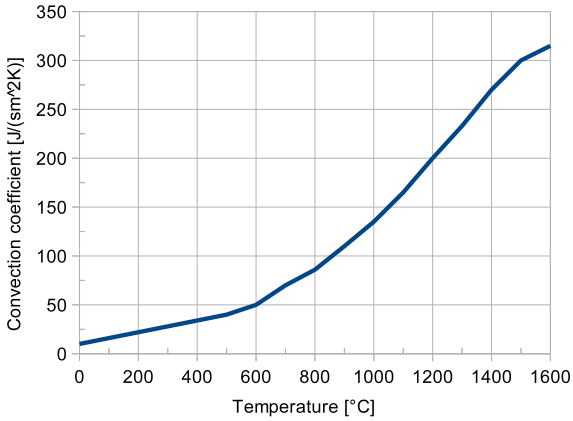

Figure 5.4: Convection coefficient [19]

To save computation time the convection boundary condition is simply applied on the outer surface near the weld zone, as it is visualized by the blue surface in Fig. 5.5. For the lower temperature range, the heat flow by radiation and convection is much smaller than the heat transport by conduction. This is why it is assumed to be only a small approximation to apply the heat boundary condition only on the surface located near the weld, which is thus exposed to higher temperatures.

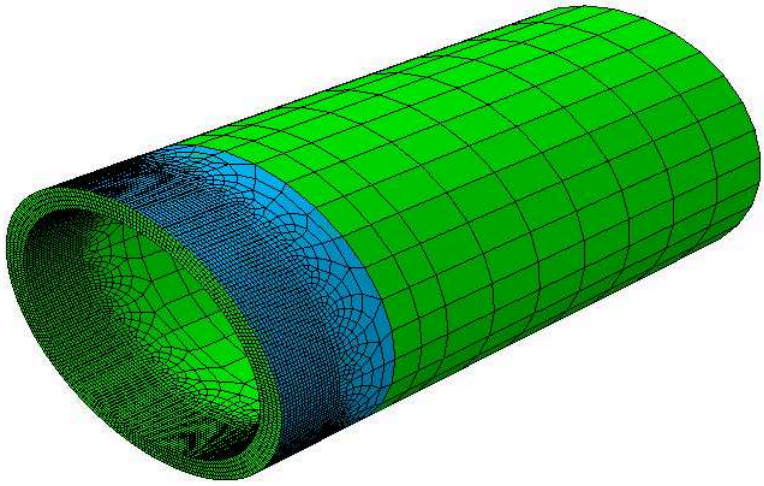

Figure 5.5: Zone where the convection boundary condition is applied

Because of the use of symmetry, no heat flux occurs across the symmetry surface. Fig. 5.6 shows the temperature distribution during the welding procedure, when the arc reaches 270° in circumferential direction. Fig. 5.7 shows the isothermes in thickness direction of the pipe. The molten area is colored in red and the actual weld is symbolized with bold black lines. With the assumptions made about the geometry of the heat source, the isothermes that define the weld geometry envelop a larger surface than the actual weld. The penetration is modeled almost realistic whereas the thickness of the weld on the surface is overestimated.

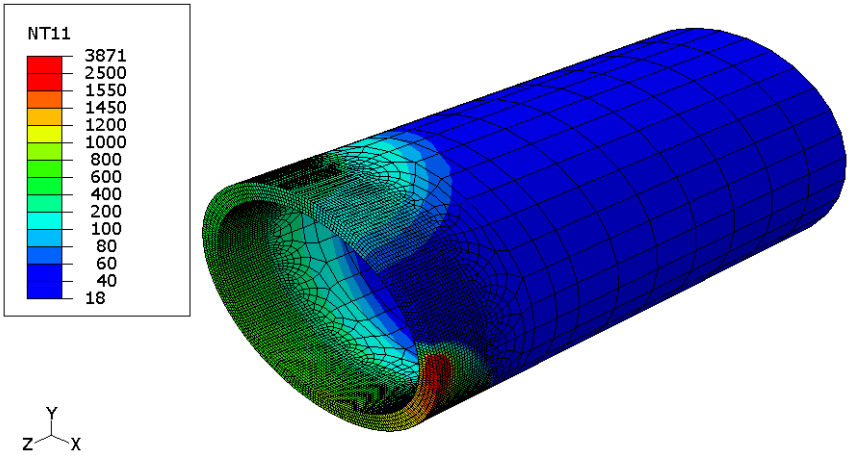

Figure 5.6: Temperature distribution during the welding process of the verification model

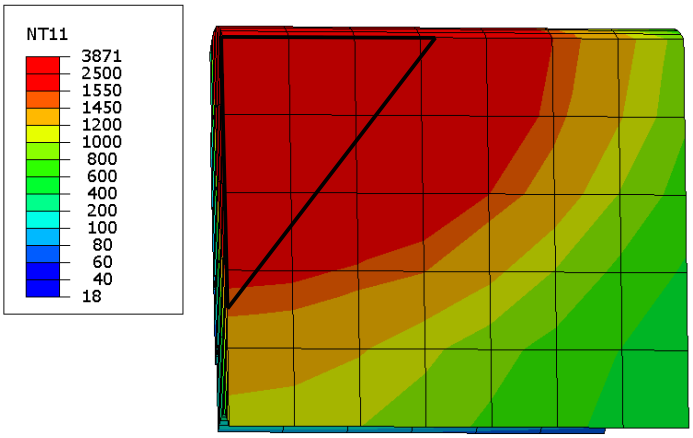

Figure 5.7: Temperature distribution and weld geometry of the verification model

For the mechanical analysis, the nodal temperature histories calculated during the thermal analysis is applied as thermal loads. The mechanical boundary conditions have also to account for the symmetry, as it is shown in Fig.4.10. After the analysis, the calculated residual stress distribtion is compared to the experimental results and the analytical solution pulished in the reference article [19]. The calculation time for the thermal and the mechanical analysis is 23 and 27 hours respectively.

Fig. 5.8 shows the hoop and the axial stress distribution on the outer surface of the pipe at 150° in circumferential direction. Both stress distributions calculated in the simulation show the same tendency as the experimental data and the analytical solution.

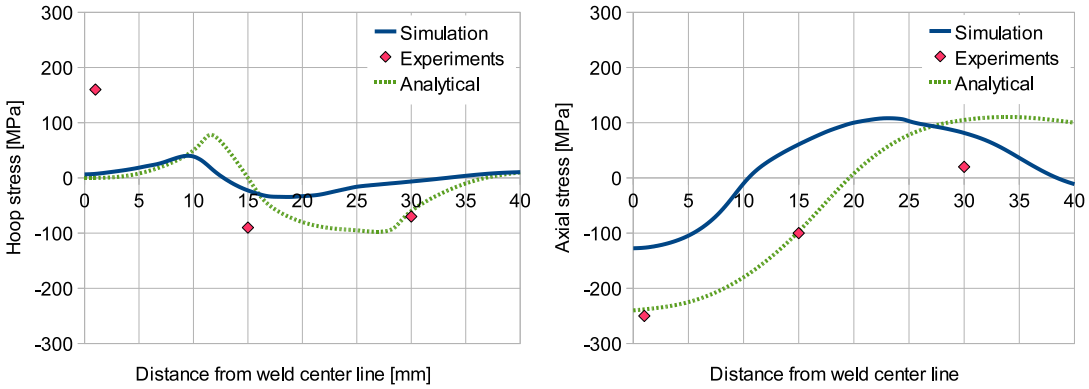

Figure 5.8: Hoop and axial stress distribution at 150° on the outer surface of the verification model

By comparing the axial stress distribution on the outer and inner surface at 150° (Fig. 5.9), it can be noted, that the stresses are opposed and thus create a bending moment, which is a typical stress distribution for welded pipes.

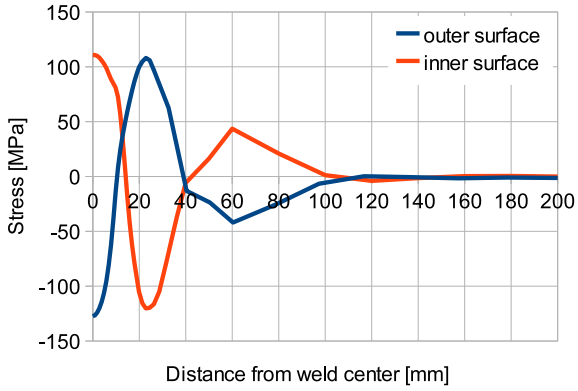

Figure 5.9: Axial stress distribution at 150° on the outer and inner surface of the verification model

In conclusion, the simulation technique seems adequate to obtain a realistic stress distribution for the simulated weld even though the chosen geometry of the heat source does not create the desired weld shape. For the following models the influence of the mechanical material data and the number of weld passes on the residual stress field was investigated by using the same simplifications as for the verification model.

5.2 Comparison of the different models

For the thermal analysis many input parameters are needed, such as the temperature dependent material properties, the boundary conditions as convection and radiation as well as the welding parameters. In this work, the principle welding parameters of heat input and welding speed could not be measured because no experimental welding procedure was conducted. For MAG-welding the heat input can be between five and 100 kJ/s and the welding speed can

be as high as 25 mm/s [34]. Due to this large range of possible input parameters, after an iterative procedure, a heat input of 13.8 kW was chosen which leads to a volumetric heat flow of 5 kW/mm^3. Because of the large weld volume, a welding speed as slow as 1.5 mm/s was estimated to be a realistic value.

For the paramteric study ten models were calculated as listed in Tab. 5.1. For a better overview the multipass models are highlighted in grey. The aim of the parametric study, is to compare the influence on the residual stress field of the *mechanical material data* and the *number of simulated weld passes*. For the study on the influence of the mechanical material data, first single-pass and multi-pass models of the two different steel grades (M1 vs. M2, and M3 vs. M4) are studied. Additionally, single-pass models using the yield strength or/and the Young's modulus deduced from the test results in Chapter 3 are developed and compared to the models with the Eurocode 3 data (M1 vs. M5, M6, M7 and M2 vs. M8, M9, M10). The models M5, M6, M7 and M8 are used in order to study the independent effects of the yield strength and the Young's modulus. Therefore in models M5 and M7, the Young's modulus of the test results and the yield strength of the Eurocode 3 is used. Conversely, in the models M6 and M8 the data for the Young's modulus is chosen from the Eurocode and the yield strength from the experimental part.

Model n°	**Parameter studied**	**n° of weld passes**	**Material**	**Yield strength**	**Young's modulus**
M1	Material	1	S355	EC3	EC3
M2	Multi-pass	3	S355	EC3	EC3
M3	Material	1	S690	EC3	EC3
M4	Material / Multi-pass	3	S690	EC3	EC3
M5	Young's modulus	1	S355	EC3	tests
M6	Yield strength	1	S355	tests	EC3
M7	Material (test data)	1	S355	tests	tests
M8	Young's modulus	1	S690	EC3	tests
M9	Yield strength	1	S690	tests	EC3
M10	Material (test data)	1	S690	tests	tests

Table 5.1: Parametric study

The diameter and wall thickness of the analysed tubes is 193.4 mm and 20 mm respectively. The dimensions of the welded tube, the shape of the weld passes for the multipass model, and the welding direction of the different passes are presented in Fig. 5.10.

According to the Eurocode 3, the thermal material behavior is the same for all the structural steel types. For the mechanical material data, only the data for the yield strength changes for the S690 compared to the model with S355. Therefore, the results of the same thermal analysis can be used for both steel types and only two thermal analyses were conducted for the ten models. For the simulation of the multi-pass model the total heat input and the welding speed is defined the same as for the single-pass model. The geometry for the weld was chosen according to the regulations in DIN9692-1 [16]. Its approximation by the single-pass and the multi-pass model is shown in Fig. 5.11.

For the calculation of the weld shape, it was assumed that the multi-pass weld covers approximately the same welding volume as the assumed single-pass weld. The heat input for the three different passes in the multi-pass model was calculated based on the surface that each weld pass covers as it is illustrated in Fig. 5.11. This leads to a heat input of 3.4

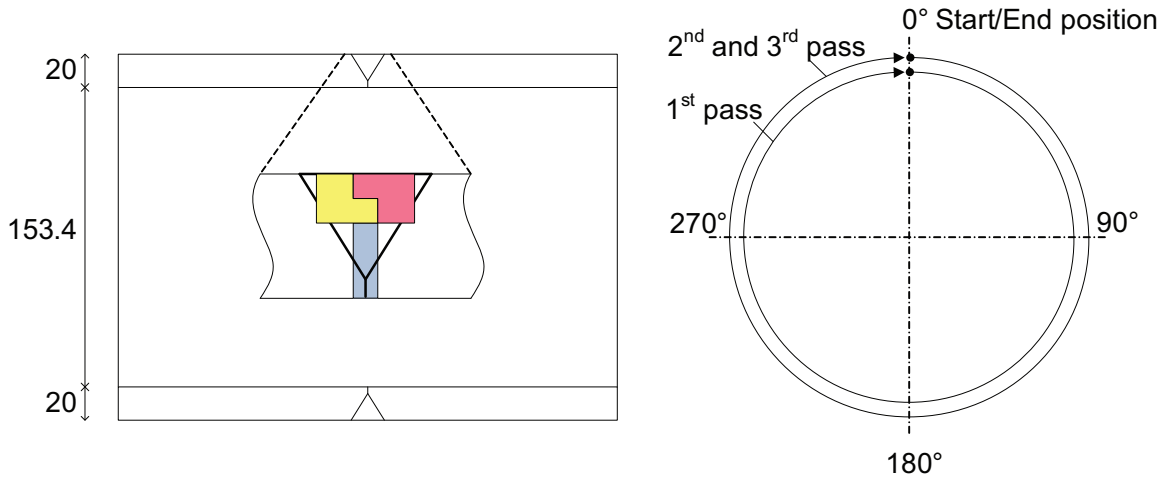

Figure 5.10: Dimensions of the welded tube, shape of the weld and welding direction of each pass

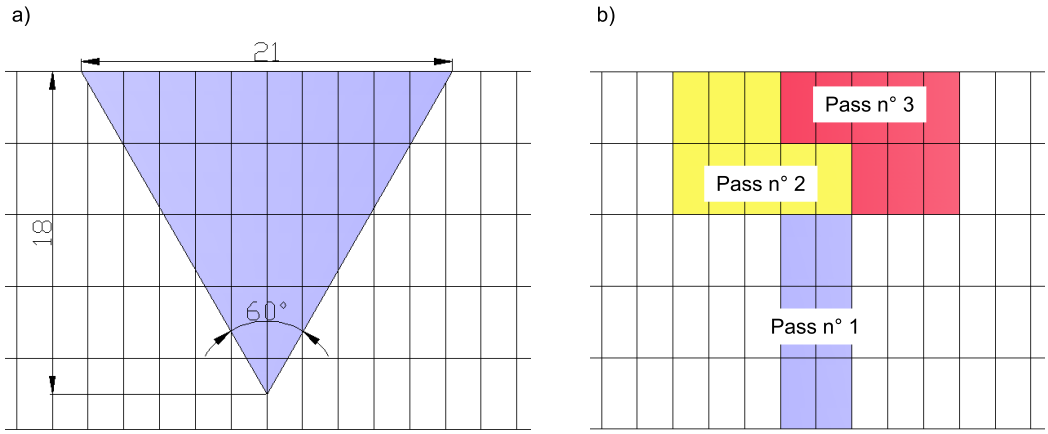

Figure 5.11: Assumed weld geometry for the different models

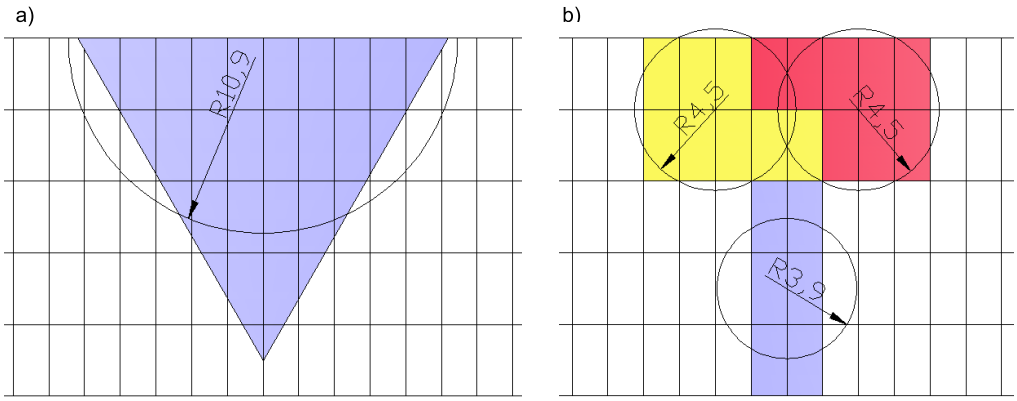

Figure 5.12: Heat source shape for the single-pass a) and multi-pass b) weld

kW for the first pass and 5.2 kW for the second and the third weld pass. Unlike the heat source shape for the simulation of the single-pass weld, an entire sphere is chosen to model the three different passes as shown in Fig. 5.12 b). The interpass time in the multi-pass model is assumed to be as long as five minutes, which seems to be a realistic value that is needed to clean the weld between the consecutive welding of the different passes. During this period, the material cools down below 200°C which is lower than the maximum temperature prescribed in welding procedure specifications for similar welds. The cooling time after the welding procedure is modeled with two hours for all ten models which leads to a relatively uniform final temperature distribution between 168 °C and 174°C for the single-pass models and between 135°C and 141°C for the multi-pass models.

The results of the thermal analysis show the isothermes and the molten area during the welding process leading to the approximation of the weld shape and the size of the heat affected zone. The temperature distribution for the single-pass and the multi-pass model are presented in Fig. 5.13 and Fig. 5.14 respectively.

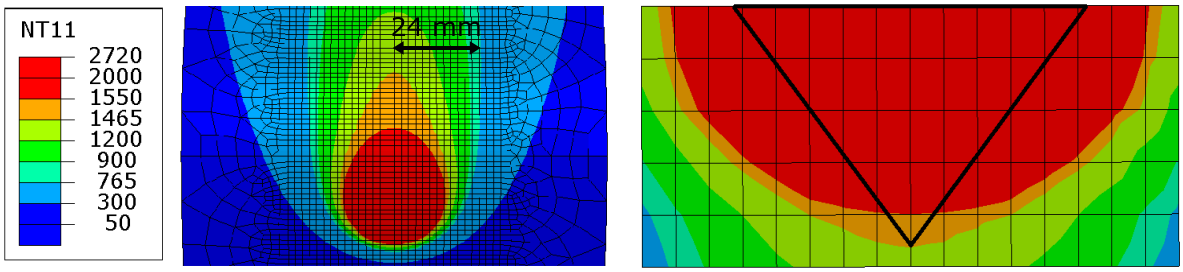

Figure 5.13: Temperature distribution in thickness direction of the single-pass weld compared to the desired weld shape

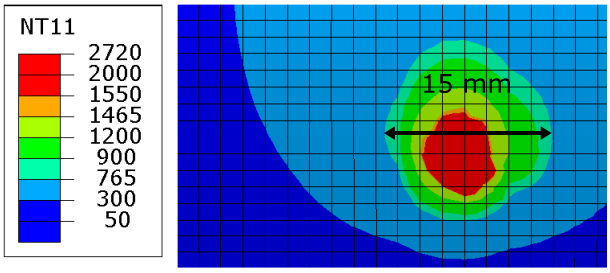

Figure 5.14: Temperature distribution in thickness direction of the third weld pass of the multi-pass weld

The single-pass model (Fig. 5.13) simulates the thickness of the weld almost exactly but the width on the surface of the tube is overestimated as it is for the verification model in chapter 5.1. The molten area in the multi-pass model (Fig. 5.15) approximates the weld shape better than in the single-pass model. By comparing the two temperature distributions it can be noticed that the molten area in the single-pass model is almost twice as large as in the multi-pass model even though the same total heat input is used. This is due to the ratio between the heat source and the element size. This also influences the regularity of the isothermes. For a large ratio as in the single-pass model the isothermes develop very uniformly around the heat source, whereas for a small ratio the spherical shape of the heat source is not approximated regularily. The heat affected zone (HAZ) is also smaller for the multi-pass

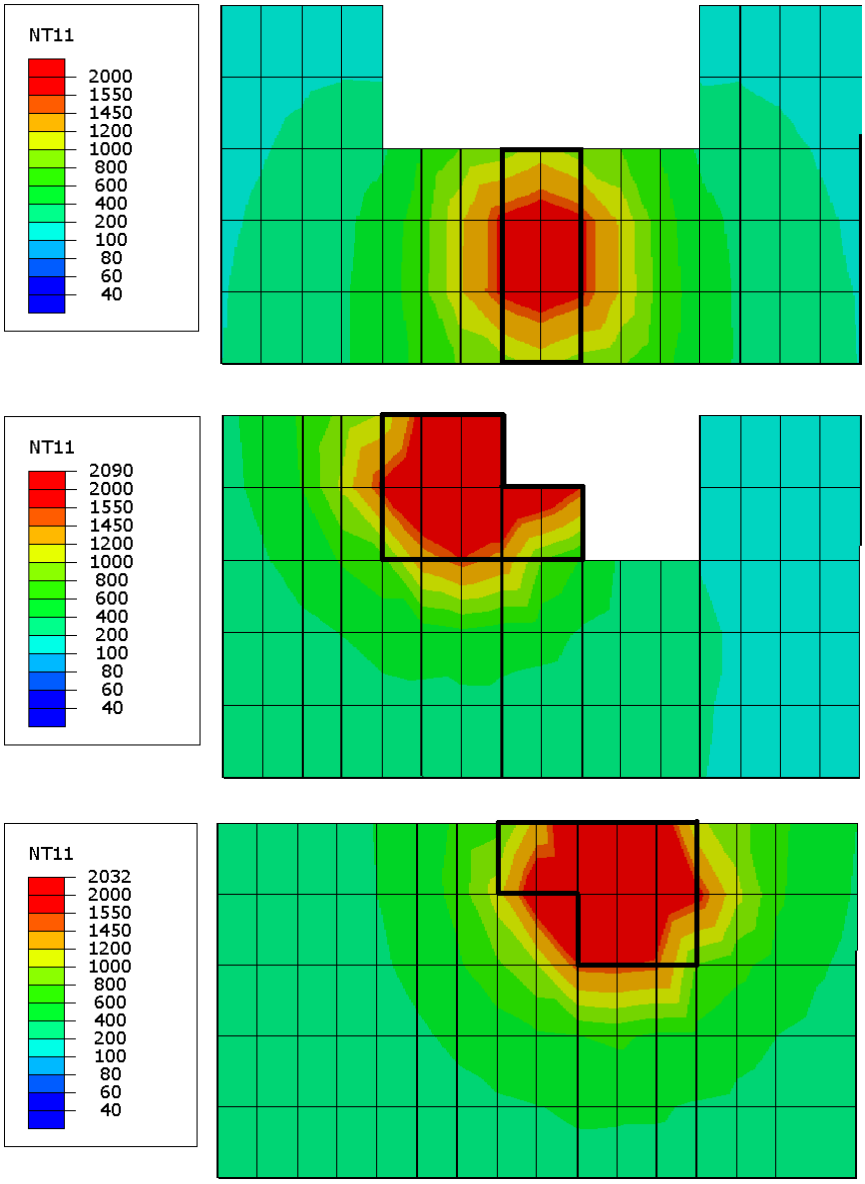

Figure 5.15: Temperature distribution in thickness direction of the multi-pass weld compared to the desired weld shape

model than for the single-pass model.

For the development of residual stresses, the time period that the material needs to cool from 800°C to 500°C is mandatory, because it can be used to approximate the microstructure that is reached during the cooling process. In many publications this time period is referred to as $t_{8/5}$. To obtain this value in the output data of an ABAQUS model, history output has to be calculated. Even if this history output is only requested for a limited number of points, a long computation time is needed. This is the reason history output was only requested for the single-pass model and only for four significant points at 0°, 90°, 180°, and 270° in the weld center line. The temperature development versus the time is presented in Fig. 5.16.

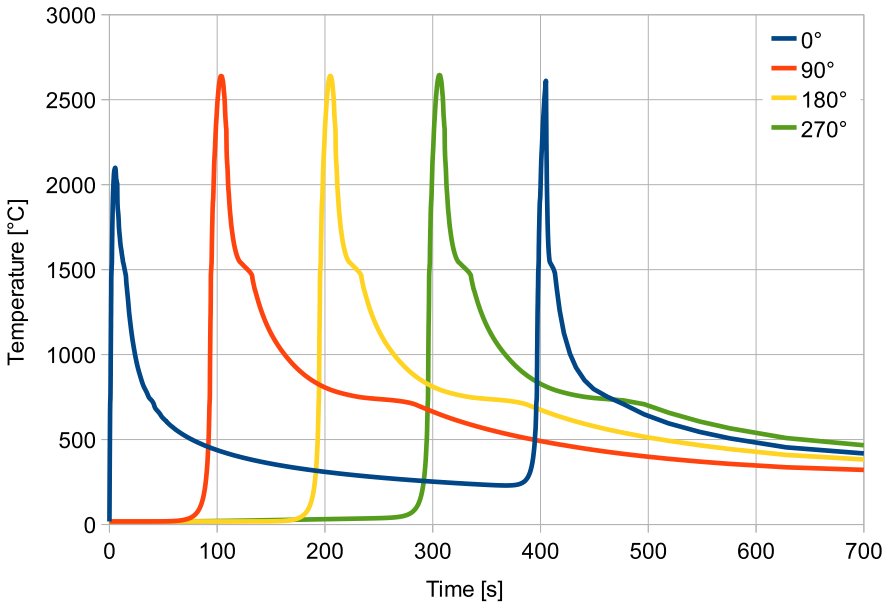

Figure 5.16: Temperature development in four points located in the weld center line

Fig. 5.16 shows that the temperature history is uniform in the weld center line except for the start-end position because the material in this zone is heated twice. This leads also to a different residual stress distribution which is why the following paragraphs focus partially on the stress distribution at the start-end position. A physical error can be noticed when comparing the temperature development at 270° and at 0°. At approximately 750°C, the temperature at 0° drops below the temperature at 270°. This error can be attributed to the simplification of the convective and radiative boundary conditions, that underestimate the cooling rate when an almost uniform temperature distribution is reached in the tubes and the heat starts to flow back to the weld region, because only in this section can heat be released to the surroundings.

The radial stresses are negligible compared to the stresses in axial and circumferential direction. Therefore, the radial stresses are not analysed in this work. The following diagrams show the significant stress distributions of the different models. More stress curves can be found in the appendix A. First, the results for the two different steel types with the material data from the Eurocode 3 [11] will be compared.

5.2.1 Influence of the material data

Fig. 5.18 shows the axial and the residual stress distribution at the weld toe of the two single-pass models with the material data taken from the Eurocode 3 [11]. The stress curves for the different yield strength have the same tendency except for the hoop stress near the start position, which is compressive for the S355 and tensile for the S690 steel. At approximately 90° in welding direction, the axial stress reaches its maximum significant difference for the two steel types.

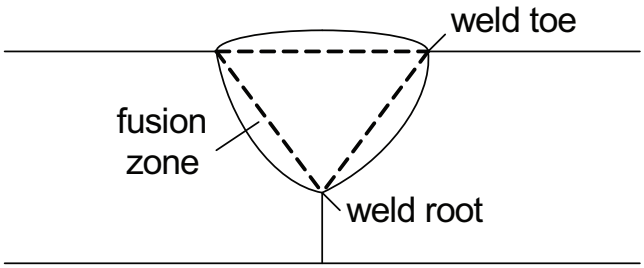

Figure 5.17: Zones in a weld

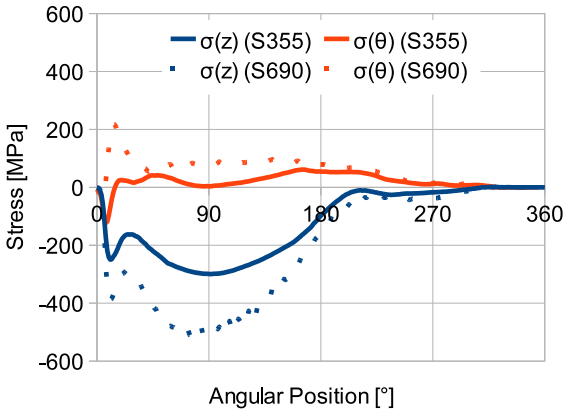

Figure 5.18: Residual stresses in circumferential direction at the weld toe of the single-pass models M1 and M3

For the single-pass models the stress distribution is symmetric to the weld center line. Consequently Fig. 5.19 presents the residual distribution at the start-end position for only half of the model. In the heat affected zone, compressive hoop stresses occur which are almost the same for the two different steel types. On the inner surface, compressive stresses occur in the heat affected zone closer to the weld and tensile residual stresses in the material located further away from the weld zone. The low residual stresses between 270° and 0° in the direction of the welding movement, suggest that the heat input is overestimated and therefore the entire tube is heated too much when the welding arc reaches the end of the weld. This leads to low stiffness in the entire section, so that the deformations at the end of the welding process are not restrained adequately.

The highest tensile stresses occur at the weld root at 90° in welding direction. Fig. 5.20 presents the stress distributions on the outer and inner surface at this circumferential location for the two single-pass models. The axial stress distribution shows that compressive stresses

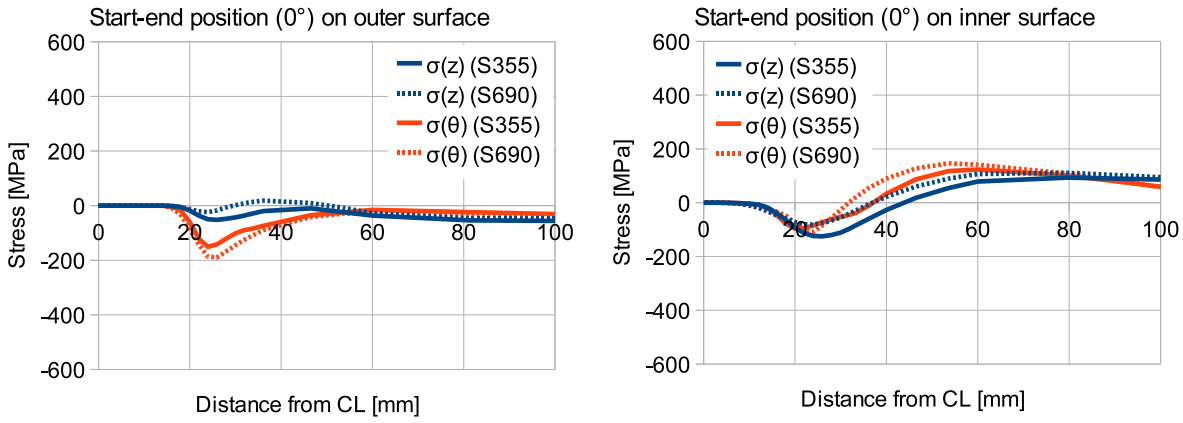

Figure 5.19: Residual stresses at the start-end position of the single-pass models M1 and M3

occur on the outside and tensile stresses on the inside of the tube, which creates a bending moment in the pipe. For the steel type S355, the stresses on the outside and the inside surface are almost exactly opposed. The axial stresses resulting from the simulation of steel type S690 are almost twice as high on the weld root and on the weld toe compared to the results of S355, whereas in the parts outside of the heat affected zone the stresses coincide. According to Radaj [35] the residual stress distribution in the entire welded component is linked to the plastic deformation in the weld zone. Thus, the stresses in the far field are not caused by thermal plastic strains but they are due to kinematic compatibilty.

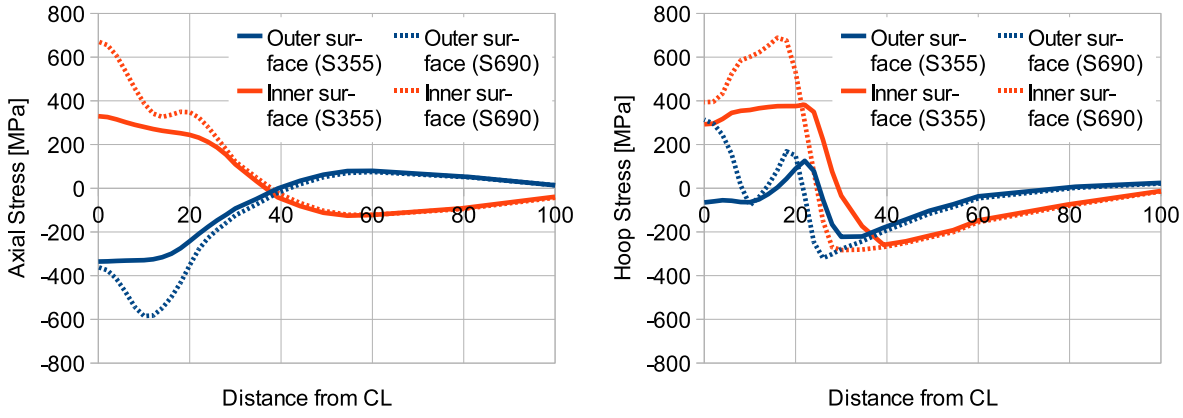

Figure 5.20: Residual stresses at 90° of the single-pass models M1 and M3

Fig. 5.21 presents the residual stresses in circumferential direction at the weld toe of the multi-pass models. The figure on the left shows the stress distribution on the weld toe located on the second weld pass and the figure on the right the stress distribution on the third weld pass respectively. The tendency of the stress distributions is the same at the two locations, but the magnitude and sign differ. In detail, the axial residual stress near the second weld pass is tensile in the first half of the tube in circumferential direction, whereas it is compressive near the third weld pass. The axial stress distribution of the two different steel types is similar, while on the contrary, the S690 model produced higher tensile hoop stresses than the model with tubes made of S355.

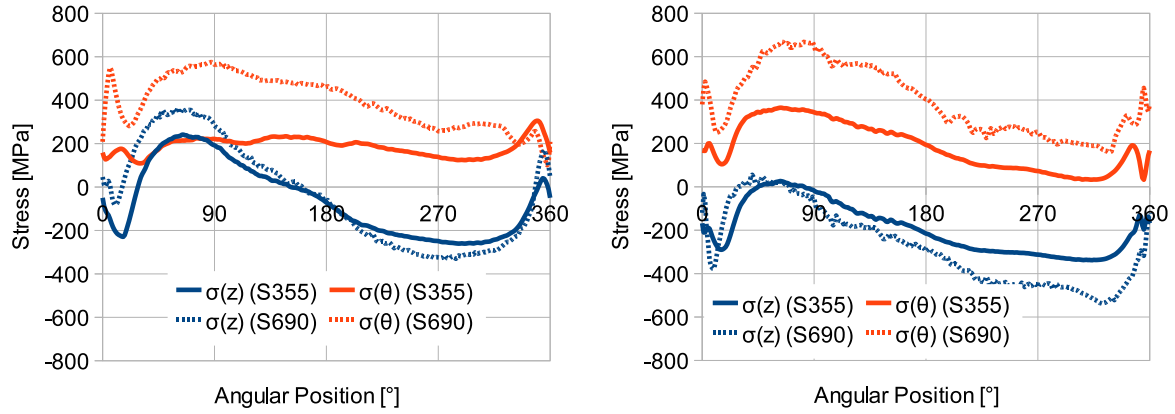

Figure 5.21: Residual stresses in circumferential direction at the weld toe of the multi-pass models

The residual stress distributions at the start-end position on the outer and the inner surface of the multi-pass models are presented in Fig. 5.22. In the diagrams, the negative distance represents the half of the tube located in the direction of the second weld pass and the positive distance represents the part near the third weld pass. The tendencies of the stress distributions is similar for the two different steel types except for the axial stress on the inner surface. Whereas the model with the steel type S355 produces sligthly tensile stresses in the molten area, while the stresses for the model with S690 are compressive.

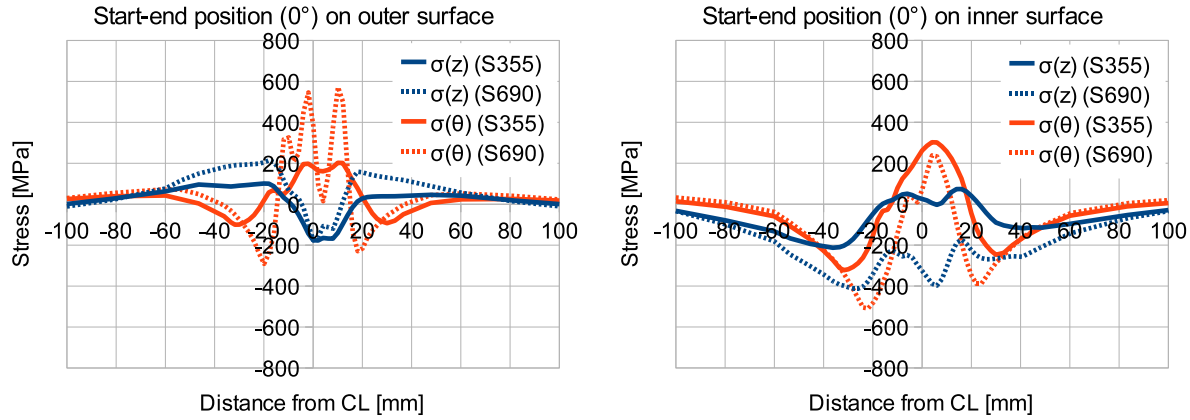

Figure 5.22: Residual stresses at the start-end position of the multi-pass models

When analysing the stress distribution at 90° on the outer and inner surface of the multi-pass models, it can be stated that at about 60 mm from the weld center line the axial stress distributions of the two different steel types start to coincide and become equivalent to zero. The hoop stresses already coincide at a distance of approximately 25 mm from the center line. The high strength steel shows increased tensile peaks of the axial and hoop stresses in the heat affected zone.

The following figures show the results for the single-pass models with the material data derived from the test results in chapter 3. For the temperatures above 1400°C the Young's modulus is set to 10 MPa and the yield strength to 1 MPa respectively. Fig. 5.24 shows the

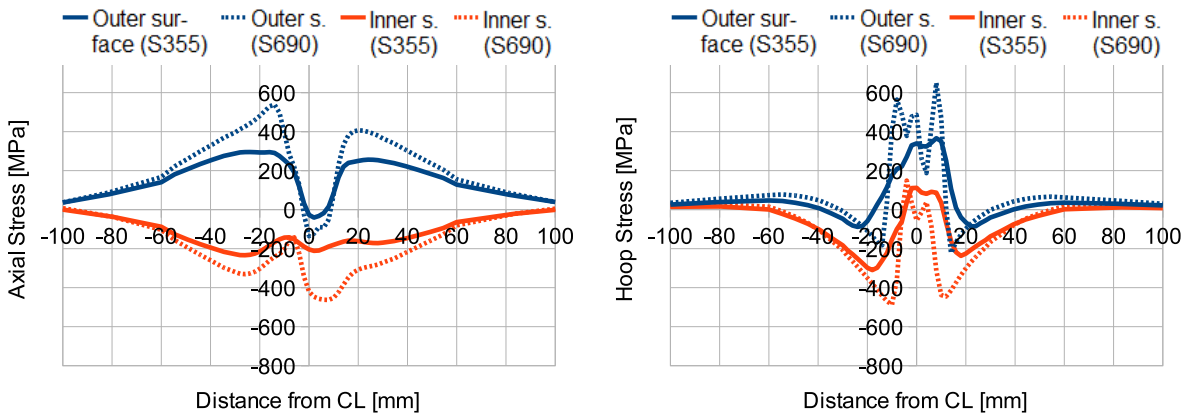

Figure 5.23: Residual stresses at 90° of the multi-pass models

stress distribution at the weld toe of different models for steel grade S355. The maximum deviation occurs for the hoop stress of model M6, where only the yield strength is changed, compared to the model with the Eurocode data. The influence of the Young's modulus from the test data reaches its maximum also in the hoop stress distribution, but it is less pronounced than for model M6. When combining the models M5 and M6, the tendency of the stress distributions remains the same for the model with the Eurocode data with a maximum deviation of 50 MPa.

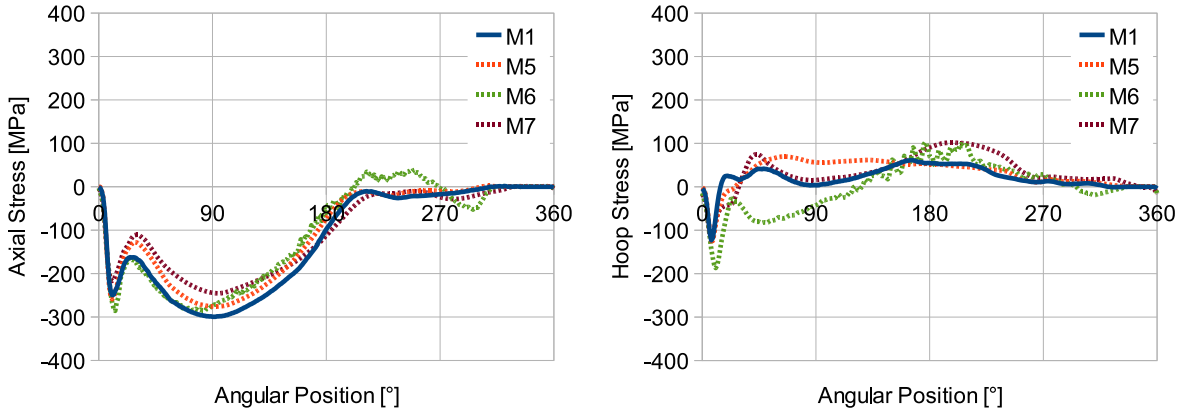

Figure 5.24: Residual stresses in circumferential direction at the weld toe of the single-pass models M1, M5, M6 and M7

Fig. 5.25 illustrates the residual stress distributions at the weld toe for the single-pass models with the steel grade S690. The tendency of the axial stress remains unchanged and the maximum derivation occurs for the model where only the Young's modulus is adapted to the test results. The tendency of the hoop stress distribution differs for the model M8, but the hoop stress in general is very low.

In conclusion it can be stated that the yield strength has a significant influence on the magnitude of the stresses in the heat affected zone but not on the general tendency of the stress distribution. The most significant difference that occured for the stress calculation between the two different steel types is presented in Fig. 5.18. The hoop stress near the start

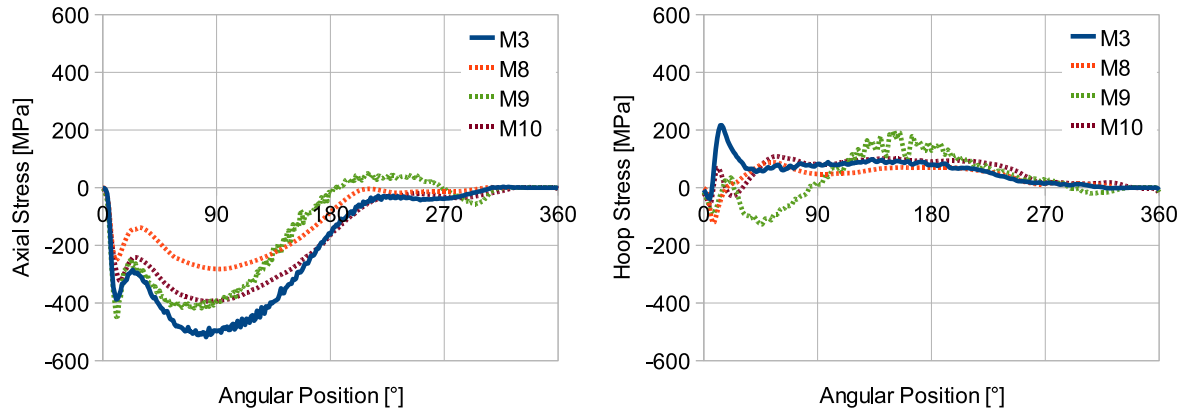

Figure 5.25: Residual stresses in circumferential direction at the weld toe of the single-pass models M3, M8, M9 and M10

position is tensile for the high strength steel and compressive for the S355. The calculation of the stresses with one steel type therefore does not allow conclusions on the stress distribution for models with a different yield strength. The mechanical data for steel at high temperatures given in the EC 3 is meant to be used for fire design and underestimates the yield strength in particular. For a realistic residual stress determination using numerical simulation it is therefore important to use an adequate material model with accurate data for the material behavior at high temperatures. The models with the Young's modulus and the yield strength from the experimental part of this work presented in Figures 5.24 and 5.25 also show the influence of the Young's modulus. It also appears, that the test data for the steel grade S690 has a stronger influence on the stress distributions than the test data for the steel grade S355. This could be interpretated as an indicator for the necessity of including the effect of phase transformation for the steel grade S690 as concluded by Wichers [47].

5.2.2 Influence of the weld-pass number

The following diagrams illustrate the difference between the use of a single-pass and a multi-pass model. The axial stress distribution at the weld toe of the single-pass model differs considerably from the axial stress distribution in circumferential direction of the multi-pass model (compare Fig. 5.26). Except at the start/end position no paralels can be found. The same statement is valid for the hoop stress distribution in circumferential direction at the weld toe. Whereas almost no hoop stresses are calculated by the single-pass model, in the multi-pass model, hoop stresses of the magnitude close to the yield strength occur between aproximately 40° and 120° in circumferential direction.

The left diagram in fig. 5.27 illustrates the residual stress distribution in the start/end position on the outer surface. The axial stress distribution on the outer surface of the single-pass and multi-pass model coincides neither in tendency nor in magnitude, whereas the hoop stress distribution on the outer surface shows the same tendeny in both models. The only convergences can be stated for the axial stress distribution on the inner surface in the molten area (compare the right diagram in Fig. 5.27).

Fig. 5.28 illustrates the axial and hoop stress distribution at 90° in circumferential direction. The stress distributions of the single-pass and multi-pass model show the same tendency but differ in magnitude. The stresses on the inside of the tubes at the heat affected zone cal-

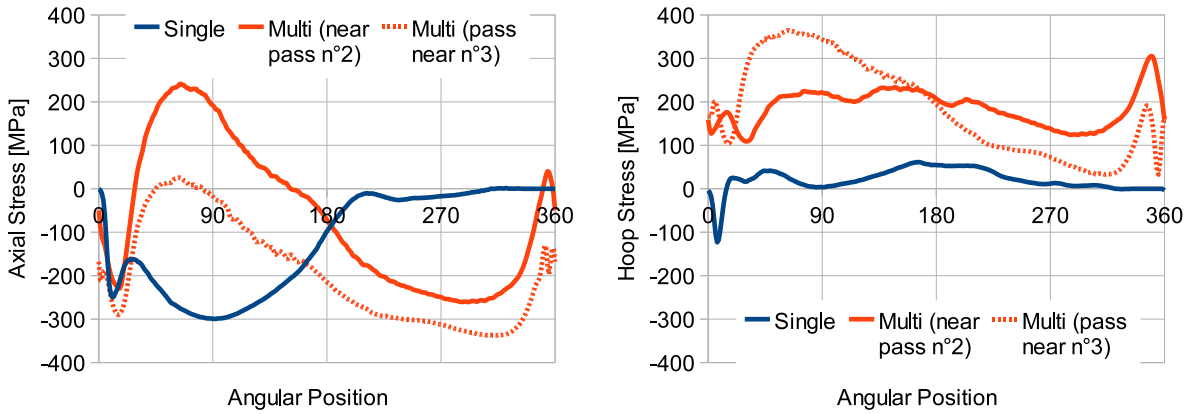

Figure 5.26: Residual stresses in circumferential direction at the weld toe of the S355 models

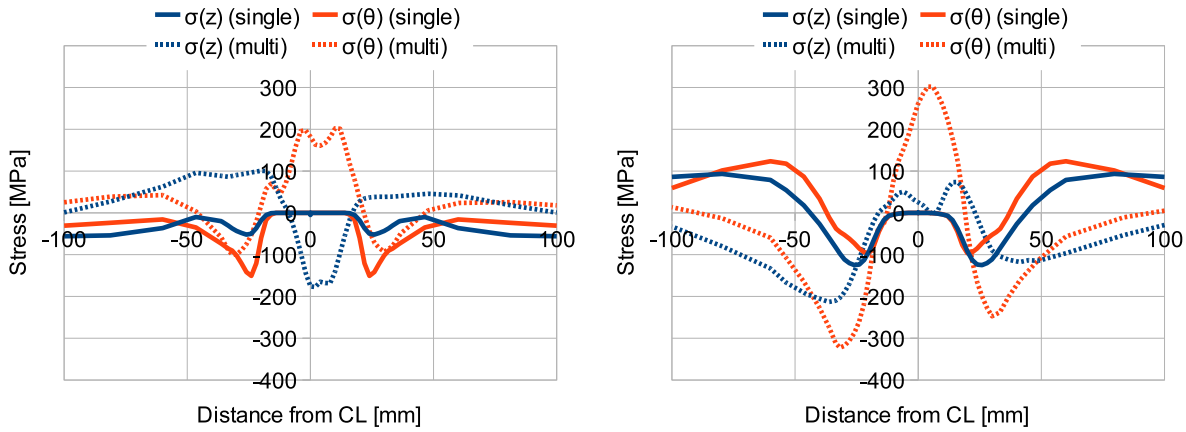

Figure 5.27: Residual stresses at the start-end position on the outer and the inner surface of the S355 models

culated by the multi-pass model are significantly lower or rather more compressive than those in the single-pass model.

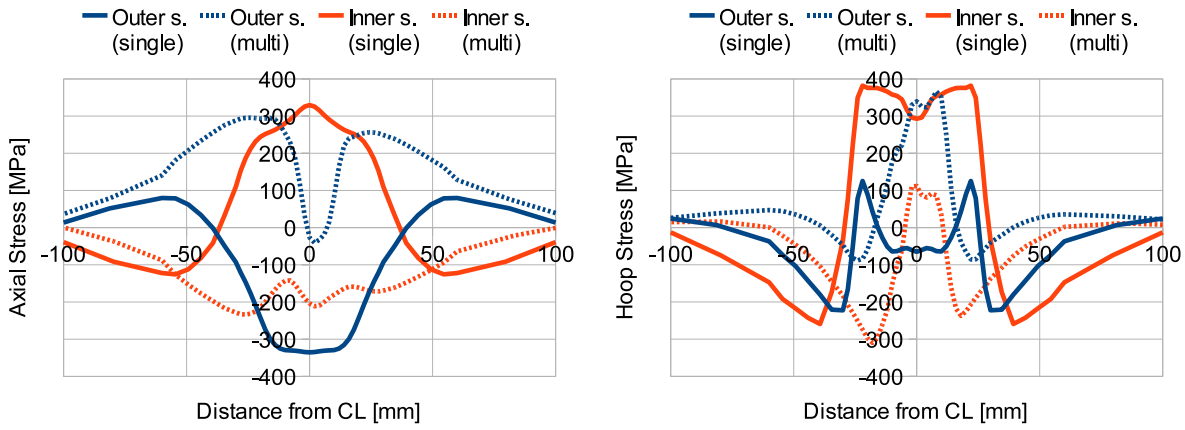

Figure 5.28: Residual stresses at 90° in circumferential direction of the S355 models

Independent from the model's steel type the conclusion can be made that a single-pass model does not simulate realistic stress distributions for a multi-pass weld. A simulation of the welding procedure with realistic weld pass numbers and welding sequence appears to be even more important than the influence of the mechanical material data. The figures for the comparison of the single- and the multi-pass model made of S690 can be found in the appendix A.5.

Chapter 6

Conclusion

In this work, the welding process and the resulting residual stress field for butt-welded tubes are studied. The aim is to simplify the model in order to save computation time, to study the influence of the mechanical material data on the residual stress distribution and the difference between a single- and a multi-pass model.

The welding simulation is realized with the finite element software Abaqus. Based on the literature study it was decided to implement exclusively three-dimensional models, because axi-symmetric models have proven in the past to be not realistic enough for the calculation of the residual stress distribution. For the simulation it is necessary to make assumptions in order to simplify the model and to reduce the calculation time. The correctness of these simplifications have a distinct influence on the quality of the results and are therefore listed below:

- No filler material is modeled and the material in the weld pool is assumed to be the same as the base metal.
- The welding arc is assumed to act on the material like a volumetric heat source with uniform density distribution.
- A constant weld speed is modeled.
- Electro-magnetic and electro-kinetic effects of the welding arc are neglected.
- No fluid flow in the weld pool is taken into consideration.
- The thermal boundary conditions are only applied on the outer surface of the tubes close to the weld.

Because no experimental welding procedure is part of the work the welding parameters are estimated which might also have an impact on the accuracy of the results. Especially for the single-pass model the chosen heat input leads to an important overestimation of the weld size. For further work an experimental welding procedure can provide more accurate parameters and lead to a realistic modeling. This is the reason why it is recommended to measure the welding paremeters and the temperature history at different locations previous to a welding simulation. As the molten area is simulated to large but not deep enough, especially for the single-pass model, a Gauss distribution could lead to a more precise simulation. However, the spherical shape of the weld source appears to be an adequate simplification. The application surface of the thermal boundary conditions, on the contrary, seems to be choosen to small.

This is concluded from the final temperature distribution and the variation of the cooling periods at different locations in the weld.

Furthermore, not only the welding process is simplified in this work, but also the material model is realized under the following assumptions:

- Both steel types have the same thermal material properties,
- The material is assumed to behave non-viscously even at high temperatures.
- A bilinear stress-strain curve is used for the material model at all temperatures.
- No effects of microstructural transformations are taken into consideration.

The bilinear stress-strain behavior is the most simplified material model for metals including plasticiy. It is more realistic to include hardening. Furthermore, steel behaves viscous at high temperatures. Accoring to the literature study it also is essential to include the effects of microstructural phase transformations, especially for high strength steel. The accuracy of the results might therefore have been influenced by the correctness of the material model. For further research, it is recommended to study the influence of a more realistic material model and to include phase transformation effects.

The accuracy of the employed material data is a major factor for the realistic description of the welding process. Therefore, the research of the thermal and especially mechanical material data at elevated temperatures of the steel grades S355 and S690 is another focus in this work. Not only the availability of the data in the high temperature range, but also the scatter due to manufacturing and differing test set-up has an important influence on the results. For the common construction steel type S355 a comprehensive study is conducted by Wichers [47]. For the high strength steel grade S690 only information on the mechanical behavior in the high temperature range is published [29]. The Eurocode 3 [11] provides thermal material data as well as temperature dependent reduction factors for the Young's modulus and the yield strength. It is valid for numerous different steel types and therefore considers the same material properties for the two steel types used in this work.

To verify the data provided by the literature, tensile tests at three different temperatures (20°C, 250°C and 800°C) are conducted in order to obtain the stress-strain curves. Based on these results, the Young's modulus and the yield strength are calculated. The results for the tests at elevated temperatures are in agreement with the data found in the literature and in Eurocode 3 for fire design of steel structures [11] except for the Young's modulus of the steel grade S355 at 800°C which is underestimated by the European standard. As for the results at room temperature, the average value of the experimental results show approximately 20 % higher results for the yield strength than the consulted standard. The Eurocode uses a 5%-factile which is on the safe side for fire contsruction, but not automatically for the residual stress calculation.

The obtained mechanical data are then used as input data for the mechnical analysis of a singlepass model and compared to the results that are obtained with the data originating from the EC 3. When analysing the residual stress distribution at the weld toe, one can notice a uniform tendency for all the models. The maximum stress derivation for the models with steel grade S355 are 70 MPa and for steel grade S690, 130 MPa respectively. However, the stress distributions for the different steel grades don't support conclusions from one stress field on the other because, in the weld and heat affected zone, they differ greatly while in the far field they coincide. These results leave unanswered whether the two steel grades

can be simulated with the bilinear material model or if the phase transformation effects can be neglected especially for the high strength steel. Furthermore, additional tests at various temperatures between 250°C and 800°C appear to be beneficial in order to verify the trend of the curves given by the Eurocode 3 and to be able to use more realistic material data in the numerical models.

The analysis regarding the quality of an approximation of a multi-pass weld by a single-pass weld reveals the important influence of the weld pass numbers on the residual stress field. Mostly, the calculated stress distributions don't show the same tendency and generally they differ greatly in magnitude. No significant similarities can be determined. Additionally, the weld pool size is largely overestimated for the single-pass model. Therefore, it can be concluded that this is an oversimplification and leads to non-realistic results.

Bibliography

[1] C. Acevedo. *Influence of residual stresses on fatigue response of welded tubular joints.* PhD thesis, Ecole Polytechnique Fédérale de Lausanne (EPFL), 2011.

[2] Z. Barsoum. Residual stress analysis and fatigue assessment of welded steel structures. *School of Engineering Sciences, Stockholm, Sweden*, 2008.

[3] U. Boese. *Das Verhalten der Stähle beim Schweißen - Teil I: Grundlagen.* DVS Media, 1995.

[4] R. Bonn. *Experimentelle und numerische Ermittlung der thermo-mechanischen Beanspruchung des Wurzelbereichs austenitischer Rundnähte.* PhD thesis, Materialprüfungsanstalt Universität Stuttgart, 2002.

[5] S. Brown and H. Song. Finite element simulation of welding of large structures. *Journal of engineering for industry*, 114(4):441–451, 1992.

[6] D. Deng and S. Kiyoshima. FEM prediction of welding residual stresses in a SUS304 girth-welded pipe with emphasis on stress distribution near weld start/end location. *Computational Materials Science*, 50(2):612–621, December 2010.

[7] D. Deng and H. Murakawa. Prediction of welding residual stress in multi-pass butt-welded modified 9Cr-1Mo steel pipe considering phase transformation effects. *Computational materials science*, 37(3):209–219, 2006.

[8] D. Deng and H. Murakawa. Numerical simulation of temperature field and residual stress in multi-pass welds in stainless steel pipe and comparison with experimental measurements. *Computational materials science*, 37(3):269–277, 2006.

[9] P. Dong. On the mechanics of residual stresses in girth welds. *Journal of pressure vessel technology*, 129:345, 2007.

[10] I. F.Z. Fanous, M. Y.A. Younan, and A. S. Wifi. Introduction of the element interaction technique for welding analysis and simulation. *Journal of pressure vessel technology*, 127: 487, 2005.

[11] Normenausschuss Bauwesen (NABau) Deutsches Institut für Normung e.V. *Eurocode 3: Bemessung und Konstruktion von Stahlbauten - Teil 1-2: Allgemeine Regeln - Tragwerksbemessung für den Brandfall*, 2006.

[12] Normenausschuss Bauwesen (NABau) Deutsches Institut für Normung e.V. *Eurocode 3: Bemessung und Konstruktion von Stahlbauten - Teil 1-9: Ermüdung*, 2006.

[13] Normenausschuss Bauwesen (NABau) Deutsches Institut für Normung e.V. *Eurocode 3: Bemessung und Konstruktion von Stahlbauten - Teil 1-12: Zusätzliche Regeln zur Erweiterung von EN 1993 auf Stahlsorten bis S700*, 2007.

[14] Normenausschuss Materialprüfung (NMP) Deutsches Institut für Normung e.V. *Metallische Werkstoffe - Zugversuch - Teil 5: Prüfverfahren bei erhöhter Temperatur*, 1992.

[15] Normenausschuss Materialprüfung (NMP) Deutsches Institut für Normung e.V. *Metallische Werkstoffe - Zugversuch - Teil 1: Prüfverfahren bei Raumtemperatur*, 2001.

[16] Normenausschuss Schweißtechnik (NAS) Deutsches Institut für Normung e.V. *Schweißen und verwandte Prozesse - Empfehlungen zur Schweißnahtvorbereitung - Teil 1: Lichtbogenhandschweißen, Schutzgasschweißen, Gasschweißen, WIG-Schweißen und Strahlschweißen von Stählen (ISO 9692Â1:2003)*, 2004.

[17] J. A. Goldak and M. Akhlaghi. *Computational welding mechanics*. Springer Verlag, 2005.

[18] J. Hildebrand. *Numerische Schweißsimulation - Bestimmung von Temperatur, Gefüge und Eigenspannung an Schweißverbindungen aus Stahl- und Glaswerkstoffen*. PhD thesis, Institut für Stahlbau, Bauhausuniversität Weimar, 2008.

[19] R. I. Karlsson and B. L. Josefson. Three-dimensional finite element analysis of temperatures and stresses in a single-pass butt-welded pipe. *Journal of pressure vessel technology*, 112:76, 1990.

[20] U. Kuhlmann, J. Bergmann, A. Dürr, R. Thumser, H. P. Günther, and U. Gerth. Erhöhung der Ermüdungsfestigkeit von geschweißten höherfesten Baustählen durch Anwendung von Nachbehandlungsverfahren. *Stahlbau*, 74(5):358–365, 2005. ISSN 1437-1049.

[21] C. H Lee and K. H Chang. Three-dimensional finite element simulation of residual stresses in circumferential welds of steel pipe including pipe diameter effects. *Materials Science and Engineering: A*, 487(1-2):210–218, 2008.

[22] Chin-Hyung Lee and Kyong-Ho Chang. Prediction of residual stresses in high strength carbon steel pipe weld considering solid-state phase transformation effects. *Computers & Structures*, 89(1-2):256–265, January 2011.

[23] L. E. Lindgren. Finite element modeling and simulation of welding part 1: Increased complexity. *Journal of thermal stresses*, 24(2):141–192, 2001.

[24] L. E. Lindgren. Finite element modeling and simulation of welding - part 2: improved material modeling. *Journal of thermal stresses*, 24(3):195–231, 2001.

[25] L. E. Lindgren. Finite element modeling and simulation of welding - part 3: efficiency and integration. *Journal of thermal stresses*, 24(4):305–334, 2001.

[26] L. Lobanov, V. Poznyakov, V. Pivtorak, O. Mikhodui, and V. Orlovskyi. Residual stresses in welded joints of high-strength steels. *Materials Science*, pages 1–11, 2009.

[27] T. Loose. *Einfluß des transienten Schweißvorganges auf Verzug, Eigenspannungen und Stabilitätsverhalten axial gedrückter Kreiszylinderschalen aus Stahl*. PhD thesis, Universität Fridericiana Karlsruhe (TH), 2007.

[28] J. Mullins and J. Gunnars. *Influence of Hardening Model on Weld Residual Stress Distribution*. Swedish Radiation Safety Authority, 2009.

[29] J. Outinen. Mechanical properties of structural steel at elevated temperatures and after cooling down. *Interscience Communications*, 2007.

[30] U. Peil and M. Wichers. Schweißen unter Betriebsbeanspruchung - Werkstoffkennwerte für einen S 355 J2G3 unter Temperaturen bis 1200° C. *Stahlbau*, 73(6):400 – 415, 2004.

[31] U. Peil and M. Wichers. Schweißen unter Betriebsbeanspruchung - Werkstoffkennwerte zur Temperaturfeldberechnung für einen S 355 J2 G3. *Stahlbau*, 74(4):249 – 257, 2005.

[32] U. Peil and M. Wichers. Schweißen unter Betriebsbeanspruchung - Numerische und experimentelle Bestimmung des Temperaturfeldes beim Schweißen. *Stahlbau*, 74(11): 843–851, 2005.

[33] Dieter Radaj. *Heat effects of welding : temperature field, residual stress, distortion*. Springer, 1992.

[34] Dieter Radaj. *Schweißprozeßsimulation : Grundlagen und Anwendungen*. Fachbuchreihe Schweißtechnik; 141. Verl. für Schweißen und Verwandte Verfahren, DVS-Verl., 1999.

[35] Dieter Radaj. *Eigenspannung und Verzug beim Schweißen: Rechen- und Meßverfahren*. DVS Media, 2001.

[36] L.O. Raymond and J. Chipman. Thermodynamic functions of iron. *Trans. Met. Soc. AIME*, 239:630–633, 1967.

[37] F. Richter. Die wichtigsten physikalischen Eigenschaften von 52 Eisenwerkstoffen. *Stahleisen - Sonderberichte*, 8, 1973.

[38] M. Siddique. *Experimental and finite element investigation of residual stresses and distortion in welded pipe and flange joints*. PhD thesis, Ghulam Ishaq Khan Institute of Engineering Sciences and Techonology, 2005.

[39] American Standard. *ASTM E21-09 - Standard Test Methods for Elevated Temperature Tension Tests of Metallic Materials*, 2009.

[40] American Standard. *ASTM E8M-09 - Standard Test Methods for Tension Testing of Metallic Materials*, 2009.

[41] D. Systèmes. Abaqus Analysis User's Manual. *ABAQUS Inc., Dassault Systèmes, France*, 2007.

[42] D. Tikhomirov, B. Rietman, K. Kose, and M. Makkink. Computing welding distortion: Comparison of different industrially applicable methods. *Advanced Materials Research*, 6-8:195–202, 2005.

[43] F. Schröter U. Kuhlmann, A. Dürr. Hochfeste Feinkornbaustähle im Stahlbau: Anwendung im Stahlbau insbesondere unter Berücksichtigung der Ermüdungsfestigkeit geschweißter Konstruktionen. Technical report, DVS, 2005.

[44] T. Ummenhofer, I. Weich, and T. Nitschke-Pagel. Lebens- und Restlebensdauerverlängerung geschweißter Windenergieanlagentürme und anderer Stahlkonstruktionen durch Schweißnahtnachbehandlung. *Stahlbau*, 74(6):412–422, 2005. ISSN 1437-1049.

[45] Normenausschuss Eisen und Stahl (FES). *DIN EN 10025 -2: Warmgewalzte Erzeugnisse aus Baustählen - Teil 2: Technische Lieferbedingungen für unlegierte Baustähle*, 2005.

[46] M. Volz. *Die Rissentstehung in statisch beanspruchten Stahlkonstruktionen unter Berücksichtigung von Schweißeigenspannung.* PhD thesis, Universität Fridericiana Karlsruhe (TH), 2009.

[47] M. Wichers. *Schweißen unter einachsiger, zyklischer Beanspruchung - Experimentelle und numerische Untersuchungen.* PhD thesis, Universitätsbibliothek Braunschweig, 2006.

[48] X. K. Zhu and Y. J. Chao. Effects of temperature-dependent material properties on welding simulation. *Computers & Structures*, 80(11):967–976, May 2002.

Appendix A

Stress distributions

A.1 Singlepass model S355 (M1)

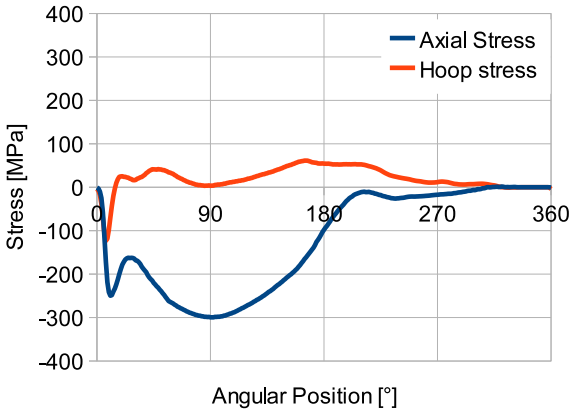

Figure A.1: Residual stresses at the weld toe in circumferential direction of the singlepass model with S355 (M1)

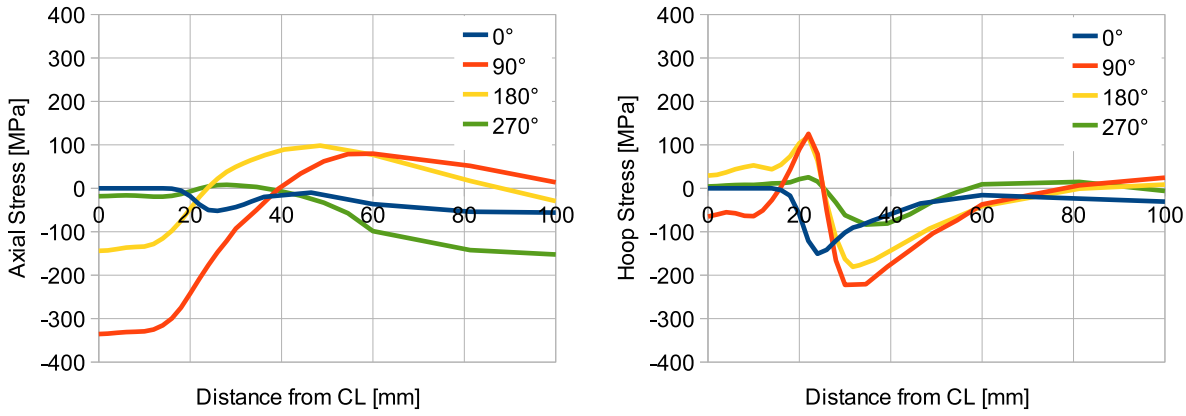

Figure A.2: Residual stresses at four positions on the outer surface of the singlepass model with S355 (M1)

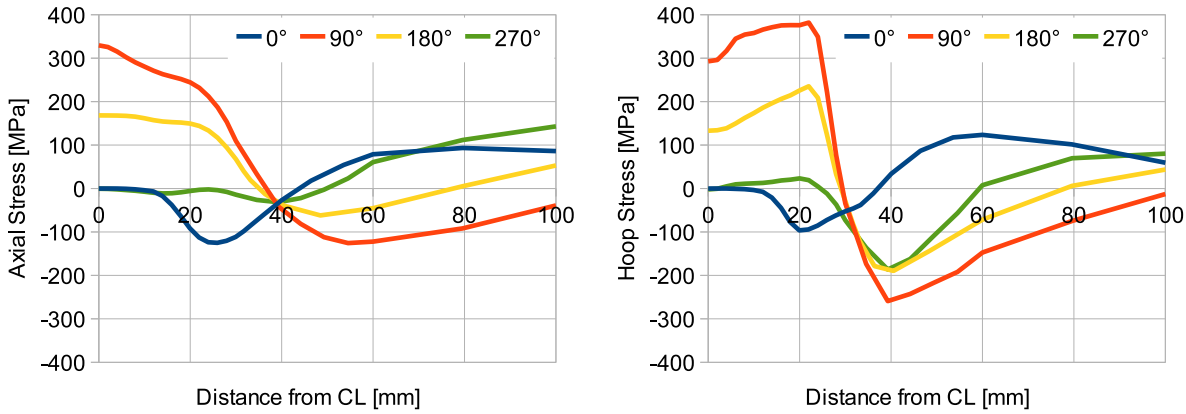

Figure A.3: Residual stresses at four positions on the inner surface of the singlepass model with S355 (M1)

A.2 Multipass model S355 (M2)

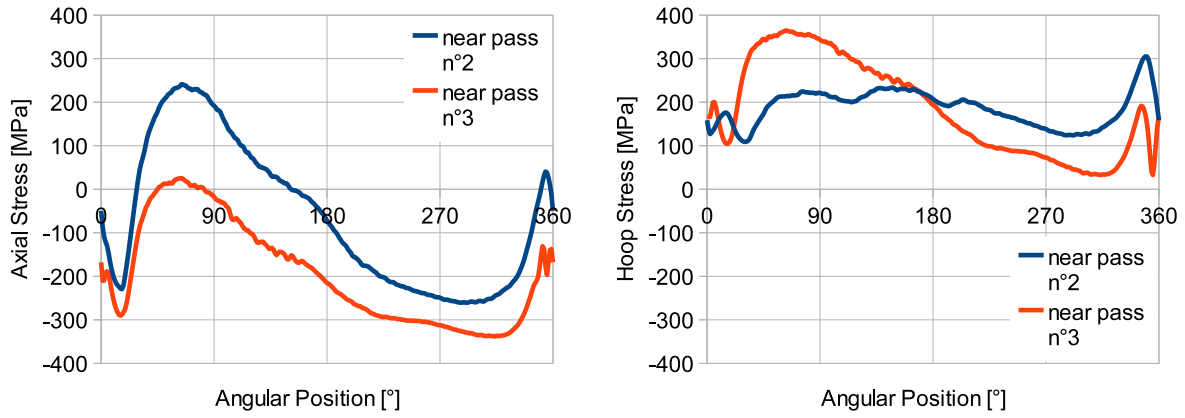

Figure A.4: Residual stresses at the weld toe in circumferential direction of the multipass model with S355 (M2)

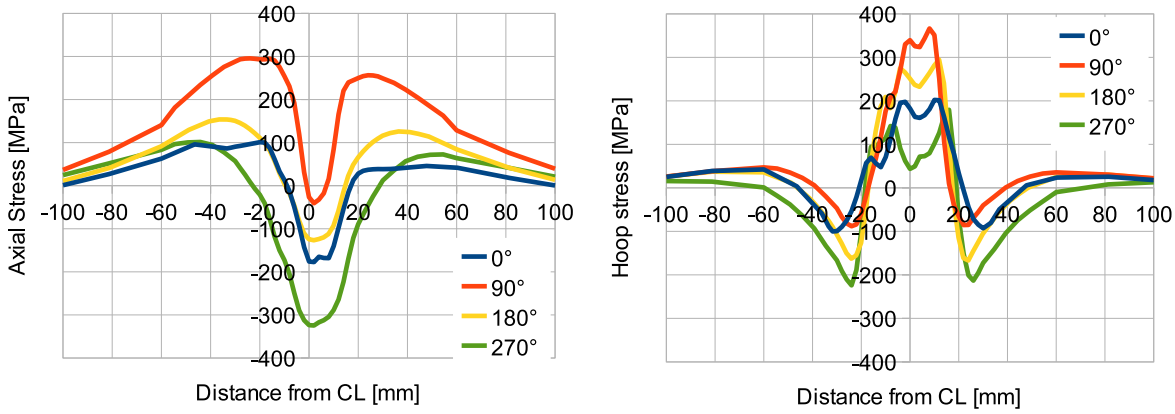

Figure A.5: Residual stresses at four positions on the outer surface of the multipass model with S355 (M2)

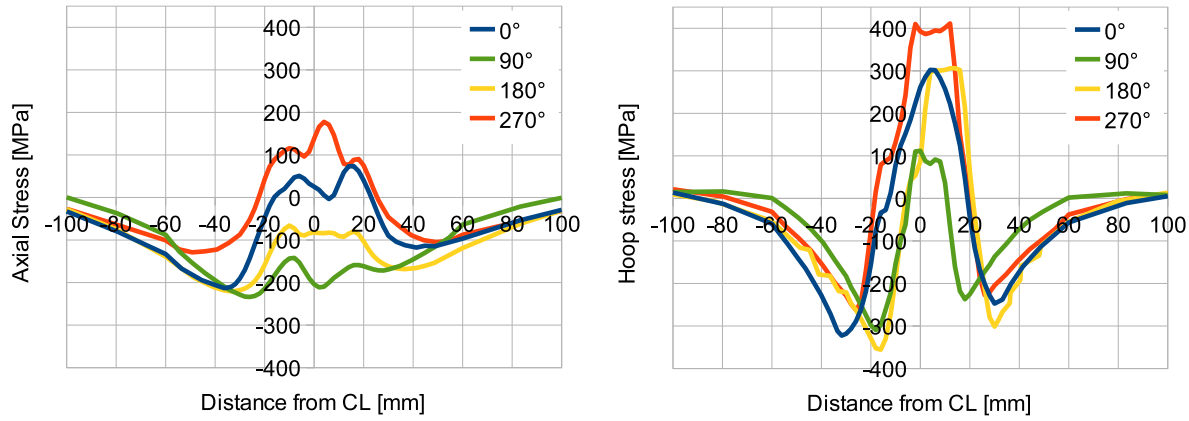

Figure A.6: Residual stresses at four positions on the inner surface of the multipass model with S355 (M2)

A.3 Singlepass model S690 (M3)

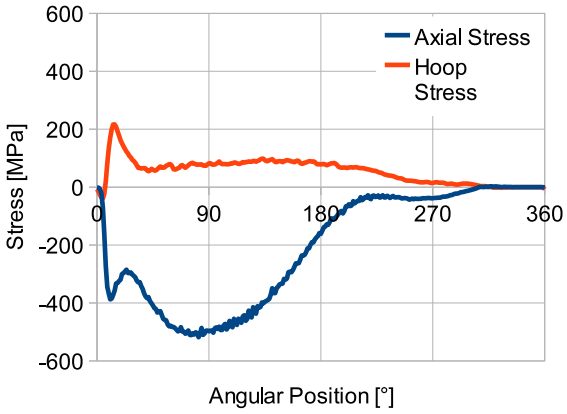

Figure A.7: Residual stresses at the weld toe in circumferential direction of the singlepass model with S690 (M3)

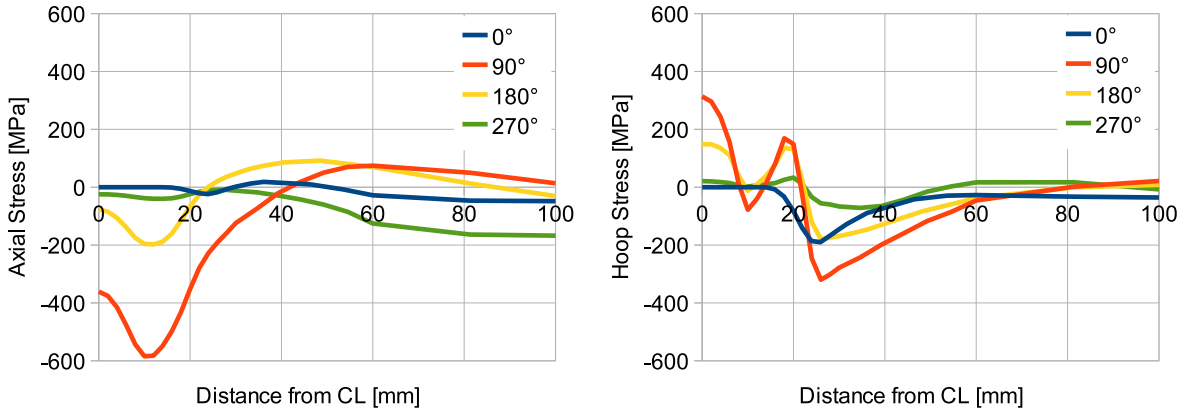

Figure A.8: Residual stresses at four positions on the outer surface of the singlepass model with S690 (M3)

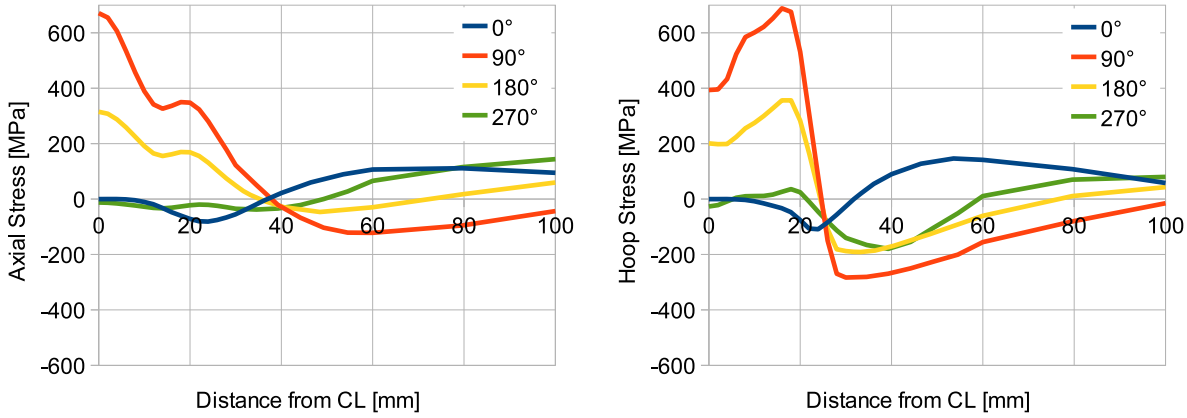

Figure A.9: Residual stresses at four positions on the inner surface of the singlepass model with S690 (M3)

A.4 Multipass model S690 (M4)

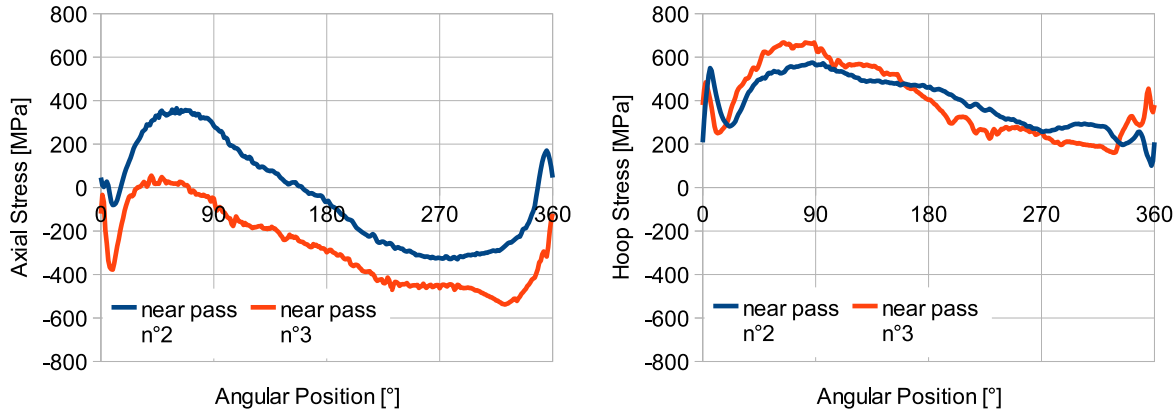

Figure A.10: Residual stresses at the weld toe in circumferential direction of the multipass model with S690 (M4)

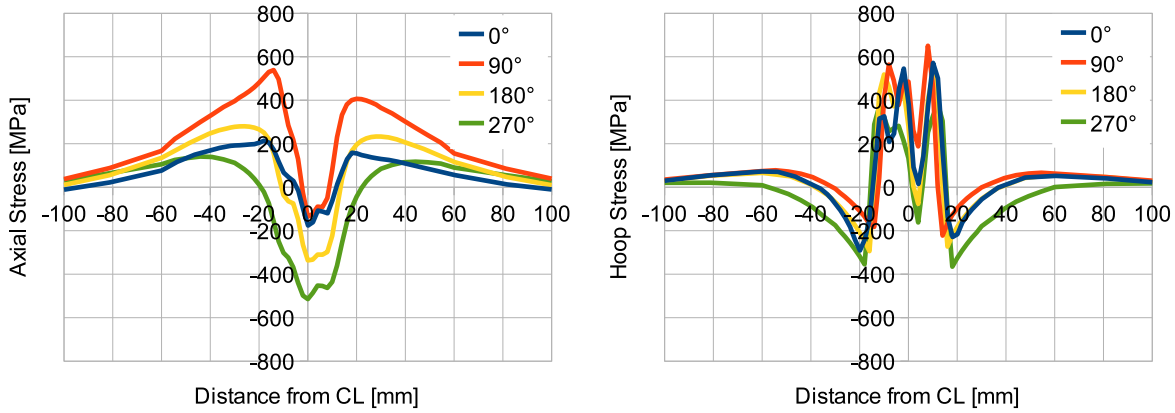

Figure A.11: Residual stresses at four positions on the outer surface of the multipass model with S690 (M4)

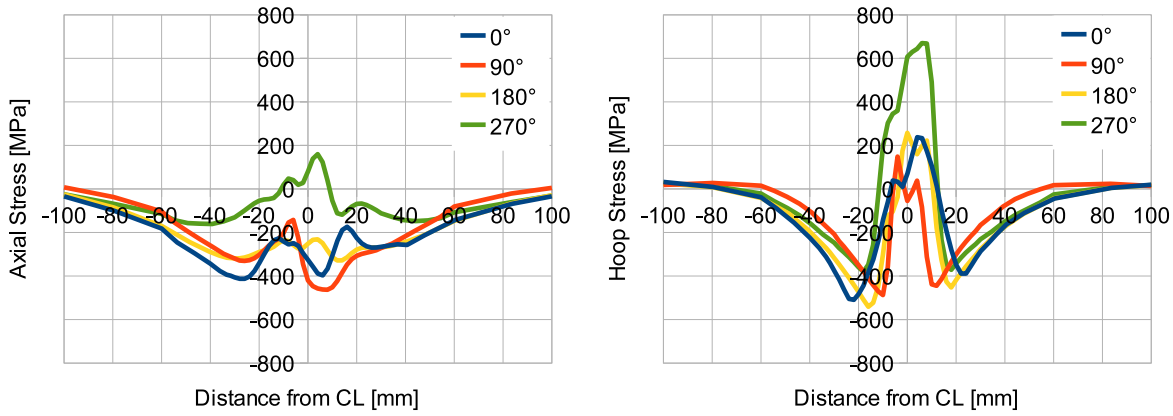

Figure A.12: Residual stresses at four positions on the inner surface of the multipass model with S690 (M4)

A.5 Single- and multipass model of S690

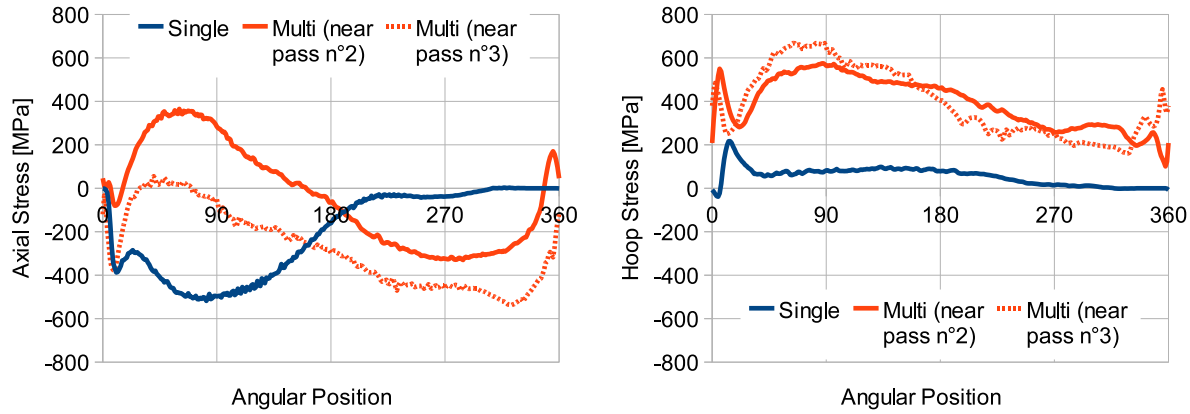

Figure A.13: Residual stresses in circumferential direction of the S690 models

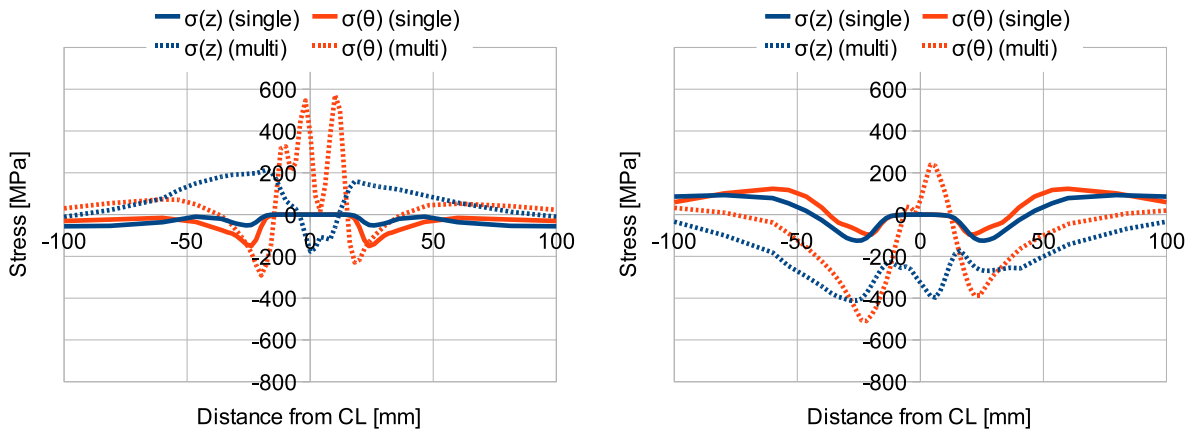

Figure A.14: Residual stresses at the start-end position of the S690 models

Appendix B

Singlepass models with test data

The Young's modulus and the yield strength for the two following models originiate from the tests presented in chapter 3. For the temperatures above 1400°C the Young's modulus is set to 10 MPa and the yield strength to 1 MPa respectively.

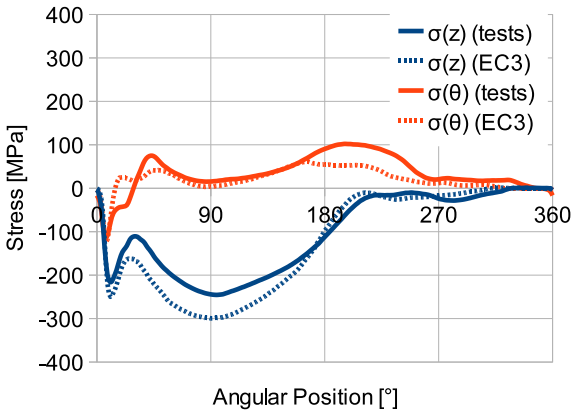

Figure B.1: Residual stresses in circumferential direction of the S355 singlepass models with test data and from the EC 3

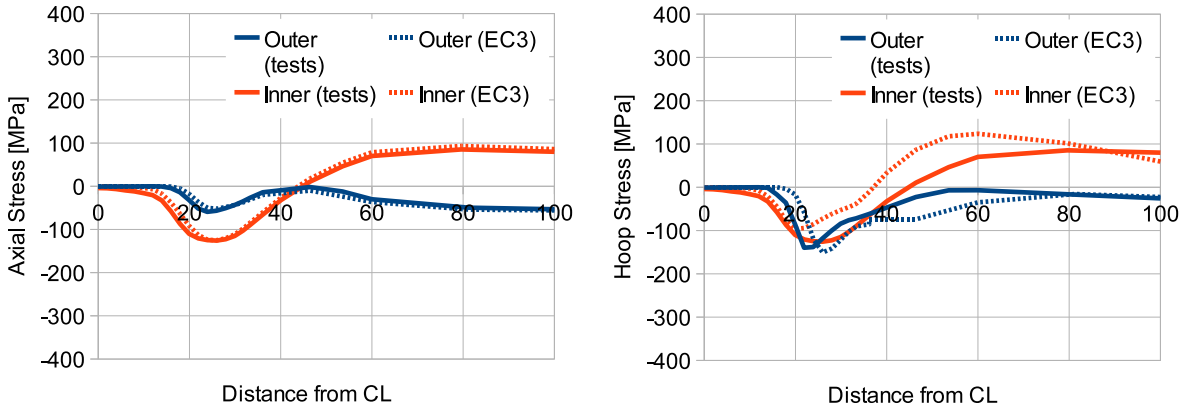

Figure B.2: Residual stresses at the start-end position of the S355 singlepass models with test data and from the EC 3

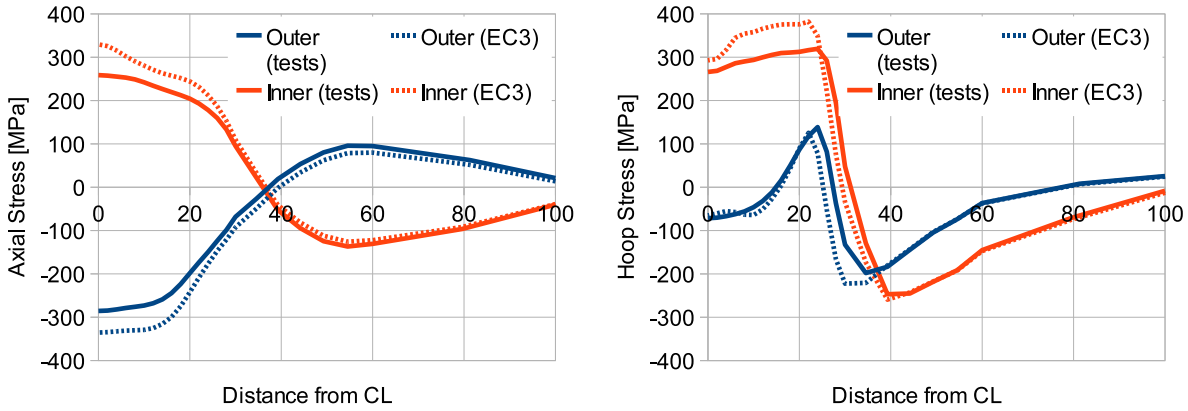

Figure B.3: Residual stresses at 90° in circumferential direction of the S355 singlepass models with test data and from the EC 3

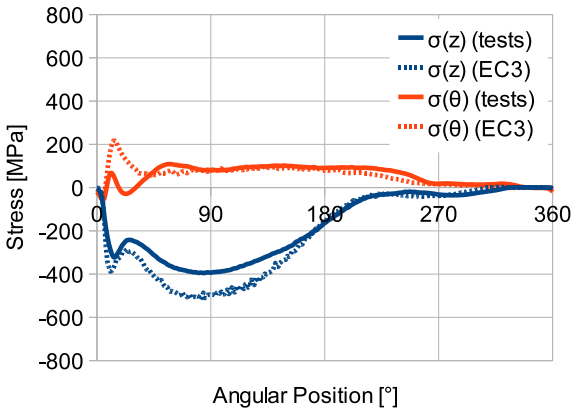

Figure B.4: Residual stresses in circumferential direction of the S690 singlepass models with test data and from the EC 3

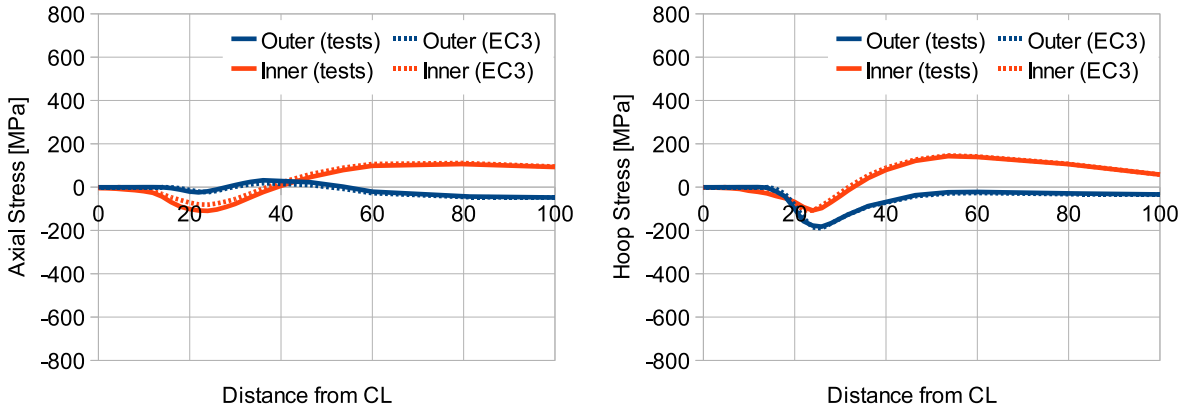

Figure B.5: Residual stresses at the start-end position of the S690 singlepass models with test data and from the EC 3

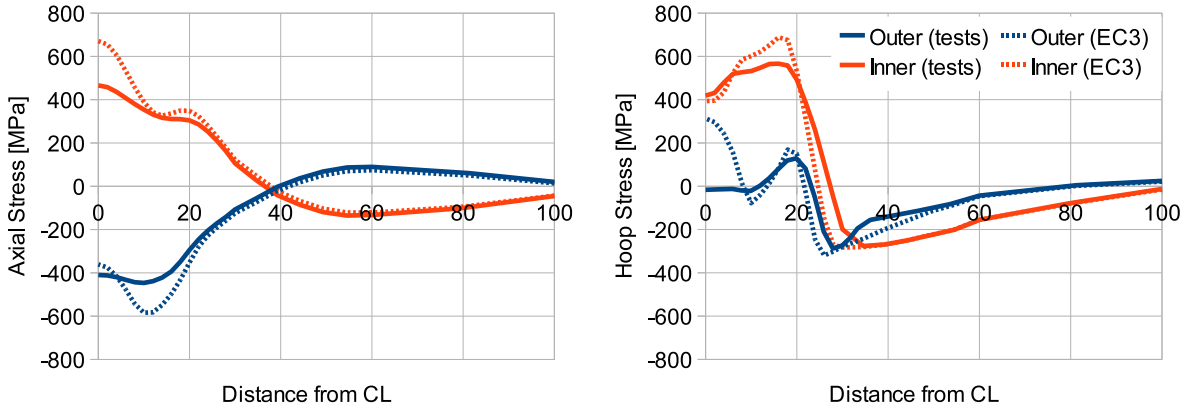

Figure B.6: Residual stresses at 90° in circumferential direction of the S690 singlepass models with test data and from the EC 3

Appendix C

FORTRAN Code for the DFLUX subroutine

```
      SUBROUTINE DFLUX(FLUX,SOL,JSTEP,JINC,TIME,NOEL,NPT,COORDS,JLTYP,
     1 TEMP,PRESS,SNAME)
c
c     subroutine for a single-pass butt weld between the tubes with the
c     dimensions:
c     diameter = 193.4 mm, thickness = 20 mm
c     total heat input: Q=13.8 kW
c     FLUX(1)  will be passed into the routine as the magnitude of the
c              flux specified as part of the element-based or surface-
c              based flux definition.
c     FLUX(2)  dq/dT, the rate of change of the flux with respect to the
c              temperature at this point, that is estimated zero in this
c              analysis.
c     SOL      the estimated value of the solution variable at this time
c              in this point.
c     KSTEP    the current step number.
c     KINC     the current increment number.
c     TIME(1)  the current value of step time.
c     TIME(2)  the current value of total time.
c     NOEL     the element number.
c     NPT      the integration point number in the element or on the
c              element's surface.
c     COORDS   the array containing the coordinates of this point.
c     JLTYP    the flux type.
c     TEMP     the current value of temperature at this integration point.
c     PRESS    the current value of the equivalent pressure stress at this
c              integration point (defined only for a mass diffusion
c              analysis).
c     SNAME    the surface name for a surface flux (JLTYP=0). (blank for
c              volume flux or an element-based surface flux)
c
c
```

```
  include 'ABA_PARAM.INC'
      DIMENSION FLUX(2),TIME(2),COORDS(3)
      DIMENSION Tstart(3), Tend(3)
      DIMENSION Tweld(3)
      DIMENSION Theta0(3)
      DIMENSION r(3)
      DIMENSION r01(3), r02(3)
      DIMENSION Vol(3)
      DIMENSION Q(3)
      DIMENSION zstart(3)

      pi=3.1416
c     number of weld passes
      n=3
c     radius' of the circles the welding arc is describing for the
c     different passes [mm]
      r(1)=82.7
      r(2)=92.7
      r(3)=92.7
c     start points in axial direction [mm]
      zstart(1)=200.
      zstart(2)=204.
      zstart(3)=196.
c     start angles
      Theta0(1)=0.
      Theta0(2)=0.
      Theta0(3)=0.
c     welding speed was estimated around 90mm/min =1.5mm/sec:
      Vweld=1.5
c     radius of the welding sphere
      r01(1)=3.91
      r01(2)=4.51
      r01(3)=4.51
c     radius square of the heat source
c     and volume of the welding sphere
      DO i=1,n
         r02(i) = r01(i)*r01(i)
         Vol(i)=4/3.*3.14*r01(i)*r01(i)*r01(i)
      ENDDO
c
c     the welding heat output [mJ/s]
      Q(1)=3400000
      Q(2)=5200000
      Q(3)=5200000
c     cooling time [s] (5 minutes)
      Tcool=300.
c     time required for one tour between 0 and 2*pi
      DO i=1,n
```

```
        Tweld(i)=2*pi*r(i)/Vweld
      ENDDO
c
c     weld start and end times
      DO i=1,n
         Tsum = 0.0
         IF (i>1) THEN
            DO j=1,(i-1)
               Tsum = Tsum + Tweld(j)
            ENDDO
         END IF
         Tstart(i)= Tsum + (i-1)*Tcool
         Tend(i) = Tstart(i)+Tweld(i)
      ENDDO
c
c     in the global coordinate system
      xx=COORDS(1)
      yy=COORDS(2)
      zz=COORDS(3)
      t=time(2)
c     loop for the different welding passes
      DO i=1,n
         IF (t.GE.Tstart(i).AND.t.LE.Tend(i)) THEN
c     angular speed, so the time has to start at zero every time
c     omega = dTheta/dt
            omega=Vweld/r(i)
c     angle: Theta = Theta(t) = integral over omega from Tstart(i) to t
            theta=omega*(t-Tstart(i))+theta0(i)
c     coordinates of the welding arc are calculated with Theta(t)
            xarc=r(i)*sin(theta)
            yarc=r(i)*cos(theta)
            zarc=zstart(i)
            r21=(xx-xarc)**2+(yy-yarc)**2+(zz-zarc)**2
            IF (r21.le.r02(i)) THEN
               flux(1)=Q(i)/Vol(i)
            EXIT
            END IF
         ELSE
            flux(1)=0.
         END IF
      ENDDO
c
      flux(2)=0.
      END
```